A FEM-based topological sensitivity approach for fast qualitative identification of buried cavities from elastodynamic overdetermined boundary data

Cédric Bellis, Marc Bonnet

A FEM-based topological sensitivity approach for fast qualitative identification of buried cavities from elastodynamic overdetermined boundary data

Cédric BELLIS and Marc BONNET
Solid Mechanics Laboratory (UMR CNRS 7649), Department of Mechanics
École Polytechnique, F-91128 Palaiseau cedex, France
{bellis,bonnet}@lms.polytechnique.fr

Abstract

A time-domain topological sensitivity (TS) approach is developed for elastic-wave imaging of media of arbitrary geometry. The TS, which quantifies the sensitivity of the misfit cost functional to the creation at a specified location of an infinitesimal hole, is expressed in terms of the time convolution of the free field and a supplementary adjoint field as a function of that specified location. Following previous studies performed under (mostly) static or time-harmonic conditions, the TS field is here considered as a natural and computationally efficient approach for defining a defect indicator function. This study emphasizes the implementation and exploitation of TS fields using standard displacement-based FEM approaches, a straightforward task once the correct sensitivity formulation is available. A comprehensive set of numerical experiments on 3-D and 2-D elastodynamic and acoustic configurations is reported, allowing to assess and highlight many features of the proposed TS-based fast qualitative identification such as its ability to identify multiple defects and its robustness against data noise.

Key words: *Inverse scattering, Time domain topological sensitivity, Adjoint solution method, Elastodynamics, Finite element method*

1 Introduction

Three-dimensional imaging of objects hidden in a solid using elastic waves is of interest in a number of applications such as nondestructive material testing or underground object detection. Such identification tasks require data provided by measurements that is overdetermined compared to what is normally necessary for solving the forward elastodynamic problem for an assumed object configuration. Minimization-based approaches that exploit the data through a misfit cost function bear considerable computational costs associated with the elastodynamic forward solver. Global optimization methods, especially, are currently impractical due to the large numbers of forward solutions entailed. More traditional gradient-based optimization is a computationally reasonable alternative for this class of inverse problems, especially when enhanced by adjoint-based shape sensitivity methods (Bonnet, 1995; Bonnet and Guzina, 2009). However, their performance depends on choosing adequately the initial guess (location, topology and geometry) of the hidden object(s).

These considerations led to the introduction of sampling methods, which aim at computing a defect indicator function in a non-iterative way from the available overdetermined data and may be defined in several ways (see the review article by Potthast, 2006) using the linear sampling method (Colton and Kirsch, 1996; Nintcheu Fata and Guzina, 2004) or the concept of topological sensitivity (TS) considered here. The TS quantifies the perturbation induced to a cost function by the creation of an object (e.g. a cavity) of vanishingly small characteristic size at a prescribed location $\boldsymbol{z}$ inside the reference (i.e. defect-free) solid as a function of the sampling point $\boldsymbol{z}$. This concept appeared in Eschenauer et al. (1994) and Schumacher (1995) in the context of topological optimization of mechanical structures, and has since also been investigated in various contexts as a method for defining a defect indicator function, see e.g. Gallego and Rus (2004); Jackowska-Strumillo et al. (2002) for 2D

elastostatics, Feijóo (2004) for 2D linear acoustics, Guzina and Bonnet (2006) for frequency-domain 3D acoustics, Bonnet and Guzina (2004) for frequency-domain 3D elastodynamics and Masmoudi et al. (2005) for 3D Maxwell equations. Moreover, the computational cost entailed by evaluating a TS field is, in general, of the order of one forward solution, and therefore modest compared to that of a standard minimization-based iterative inversion methodology. The concept of topological sensitivity is closely related to the broader class of asymptotic methods, where unknown defects whose geometry involves a small parameter are sought by means of expansions of the forward solution (rather than the misfit function) with respect to that parameter, see (e.g. Ammari and Kang, 2004, 2006).

Defect identification using TS under transient dynamical conditions have so far been the subject of only a few investigations, notably Dominguez et al. (2005) where the connection with time-reversal is explored, Bonnet (2006) in which an adjoint-based form of the TS is derived for 3-D elastodynamics and acoustics, Malcolm and Guzina (2008) and Chikichev and Guzina (2008) where the case of penetrable inclusions in acoustic and elastic media (respectively) is considered, and Bellis and Bonnet (2009) which is devoted to a specialized formulation for crack identification problems. This article addresses defect identification in elastic solids by means of the TS function defined for small-cavity nucleation in the context of 3-D time-domain elastodynamics. In a previous publication (Bonnet, 2006), the TS function was obtained as a bilinear expression featuring the (time-forward) free field and the (time-backward) adjoint solution by considering the asymptotic behavior of a system of governing integral equations based on the transient full-space elastodynamic Green's tensor, the corresponding (analogous and simpler) formulation for scalar waves was derived as a by-product, and a semi-analytical example based on transient 3-D acoustic data was presented. As in many other derivations of TS formulations published thus far, the integral-equation setting is convenient for performing the mathematical asymptotic analysis but is then just one of several possible approaches for doing numerical computations once the necessary formulae are established.

The intended contributions of this article are two-fold. Firstly, on the theoretical side, the derivation of the TS field proposed in Bonnet (2006) is clarified and extended as follows: (a) the validity of the previously-established asymptotic behaviour of the time-domain governing integral equation (and hence of the resulting TS formulation) is shown to depend on smoothness assumptions on the free field, an issue not touched upon in Bonnet (2006); (b) a simpler and more compact version of the derivation, using Green's tensors rather than full-space fundamental solutions, is presented; (c) proofs are also given for two-dimensional problems. Secondly, a comprehensive set of numerical experiments, including 3-D elastodynamic examples, is reported and discussed. Unlike previous publications where the time-domain TS is computed by means of specialized techniques based on Green's tensors, this study emphasizes the implementation and exploitation of TS fields using the standard displacement-based FEM, and indeed the ease of doing so once the correct sensitivity formulation is available. To the authors' best knowledge, this article presents the first comprehensive numerical study of TS-based defect identification methodology in time-dependent 3-D settings and implemented within general-purpose computational environments.

This article is organized as follows. The forward and inverse problems of interest are reviewed in Section 2. Topological sensitivity is defined and established, in both direct and adjoint-based forms, in Section 3, the more technical parts of the derivations being deferred to Appendix A for ease of reading. Section 4 then discusses some important features of the methodology and introduces additional concepts and notations pertaining to the FEM-based implementation and its exploitation in subsequently presented numerical results. Then, the results of FEM-based numerical experiments are presented and discussed in Sections 5 (2-D scalar wave equation) and 6 (3-D and 2-D elastodynamics).

2 Cavity identification model problem

Let Ω denote a finite elastic body in $\mathbb{R}^{\mathrm{D}}$ ($d = 3$ or $d = 2$), bounded by the external surface S and characterized by the shear modulus μ, Poisson's ratio ν and mass density ρ, and referred in the following as the *reference body*. A cavity (or a set thereof) B bounded by the closed traction-free surface(s) Γ is embedded in Ω. The external surface S, which is identical for the reference domain Ω and the cavitated domain $\Omega(B) = \Omega \setminus B$, is split into a Neumann part S_{N} and a Dirichlet part

$S_{\rm D}$, respectively associated with prescribed time-varying tractions $\bar{\boldsymbol{t}}$ and displacements $\bar{\boldsymbol{u}}$. Under this dynamical loading, an elastodynamic state $\boldsymbol{u}_B$ arises in $\Omega(B)$, which satisfies the following set of field equations, boundary and initial conditions (hereinafter referred to for generic B as $\mathcal{P}(B)$):

$$\mathcal{P}(B):\left\{\begin{array}{ll}\big[\mathcal{L}\boldsymbol{u}_B\big](\boldsymbol{\xi},t)=\boldsymbol{0} & (\boldsymbol{\xi}\in\Omega(B),t\geqslant 0)\\ \boldsymbol{t}[\boldsymbol{u}_B](\boldsymbol{\xi},t)=\boldsymbol{0} & (\boldsymbol{\xi}\in\Gamma,t\geqslant 0)\\ \boldsymbol{t}[\boldsymbol{u}_B](\boldsymbol{\xi},t)=\bar{\boldsymbol{t}}(\boldsymbol{\xi},t) & (\boldsymbol{\xi}\in S_{\rm N},t\geqslant 0)\\ \boldsymbol{u}_B(\boldsymbol{\xi},t)=\bar{\boldsymbol{u}}(\boldsymbol{\xi},t) & (\boldsymbol{\xi}\in S_{\rm D},t\geqslant 0)\\ \boldsymbol{u}_B(\boldsymbol{\xi},0)=\dot{\boldsymbol{u}}_B(\boldsymbol{\xi},0)=\boldsymbol{0} & (\boldsymbol{\xi}\in\Omega(B))\end{array}\right. \tag{1}$$

where $\boldsymbol{\xi}$ and t denotes the position vector and the time; $\mathcal{L}$ denotes the governing Navier space-time partial differential operator defined by

$$\mathcal{L}\boldsymbol{w}(\boldsymbol{\xi},t)=\nabla\cdot\boldsymbol{\sigma}[\boldsymbol{w}](\boldsymbol{\xi},t)-\rho\ddot{\boldsymbol{w}}(\boldsymbol{\xi},t) \tag{2}$$

where $\boldsymbol{\sigma}[\boldsymbol{w}]=\boldsymbol{\mathcal{C}}:\boldsymbol{\nabla}\boldsymbol{w}$ denotes the elastic stress tensor associated with a displacement $\boldsymbol{w}$, the fourth-order elasticity tensor $\boldsymbol{\mathcal{C}}$ being given (for isotropic materials) by

$$\boldsymbol{\mathcal{C}}=2\mu\left[\boldsymbol{\mathcal{I}}^{\rm sym}+\frac{\nu}{1-2\nu}\boldsymbol{I}\otimes\boldsymbol{I}\right] \tag{3}$$

(with $\boldsymbol{\mathcal{I}}^{\rm sym}$ and $\boldsymbol{I}$ respectively denoting the symmetric fourth-order and the second-order identity tensors), $\boldsymbol{t}[\boldsymbol{w}]=\boldsymbol{\sigma}[\boldsymbol{w}]\cdot\boldsymbol{n}$ is the traction vector associated with $\boldsymbol{w}$ ($\boldsymbol{n}$ being the unit normal on $S\cup\Gamma$ oriented outward from $\Omega(B)$), and $\dot{(\,)}$ and $\ddot{(\,)}$ indicate first- and second-order time derivatives.

Cavity identification problem. The location, topology and geometry of an unknown cavity system $B^{\rm true}$ (or equivalently $\Gamma^{\rm true}$) is sought by exploiting measured values of the response of the flawed solid $\Omega^{\rm true}=\Omega(B^{\rm true})$ arising due to the probing excitation. Specifically, the displacement $\boldsymbol{u}^{\rm obs}$ induced in $\Omega^{\rm true}$ by $(\bar{\boldsymbol{u}},\bar{\boldsymbol{t}})$ is monitored over the measurement surface $S^{\rm obs}\subset S_{\rm N}$ and time interval $t\in[0,T]$ (other possibilities, e.g. finite sets of measurement locations and/or times, being also allowed by the ensuing treatment). Ideally, a defect configuration $B^{\rm true}$ such that

$$\boldsymbol{u}^{\rm true}(\boldsymbol{\xi},t)=\boldsymbol{u}^{\rm obs}(\boldsymbol{\xi},t)\qquad\qquad(\boldsymbol{\xi}\in S^{\rm obs},\ 0\leqslant t\leqslant T) \tag{4}$$

is sought, where $\boldsymbol{u}^{\rm true}$ solves problem $\mathcal{P}(B^{\rm true})$ defined by (1). In practice, due to many factors (e.g. incomplete and/or inexact measurements, modelling uncertainties), the cavity is sought so as to minimize a misfit cost functional which is naturally (in the present context) expressed as a double integral over the measurement surface and the experiment duration:

$$\mathbb{J}(\Omega(B),T)=\int_0^T\int_{S^{\rm obs}}\varphi[\boldsymbol{u}_B(\boldsymbol{\xi},t),\boldsymbol{\xi},t]\,{\rm d}S_\xi\,{\rm d}t \tag{5}$$

where $\Omega(B)$ is a trial cavitated solid defined by the trial cavity B, $\boldsymbol{u}_B$ solves problem $\mathcal{P}(B)$ defined by (1), and the misfit function φ is chosen so as to define a distance between $\boldsymbol{u}_B$ and $\boldsymbol{u}^{\rm obs}$. Numerical experiments presented herein are based on the commonly-used least squares misfit function:

$$\varphi[\boldsymbol{w},\boldsymbol{\xi},t]=\frac{1}{2}|\boldsymbol{w}-\boldsymbol{u}^{\rm obs}(\boldsymbol{\xi},t)|^2 \tag{6}$$

3 Topological sensitivity

3.1 Small-cavity asymptotics

The topological sensitivity of the cost functional (5) is defined as its sensitivity with respect to the creation of an infinitesimal object of characteristic size ε at a given location $\boldsymbol{z}$ in Ω. Here, such infinitesimal object is taken to be a trial cavity $B_\varepsilon(\boldsymbol{z})$, defined by $B_\varepsilon(\boldsymbol{z})=\boldsymbol{z}+\varepsilon\mathcal{B}$ in terms of its

center $\boldsymbol{z}$, its shape specified by the unit bounded set $\mathcal{B} \subset \mathbb{R}^{\mathrm{D}}$ (with boundary $\mathcal{S}$ and volume $|\mathcal{B}|$) containing the origin, and its radius $\varepsilon > 0$. The corresponding trial cavitated solid is denoted $\Omega_\varepsilon(\boldsymbol{z})$. Following Sokolowski and Zochowski (1999) or Garreau et al. (2001), one seeks the asymptotic behavior of $\mathbb{J}(\Omega_\varepsilon(\boldsymbol{z}), T)$ as $\varepsilon \to 0$ through the expansion:

$$\mathbb{J}(\Omega_\varepsilon(\boldsymbol{z}), T) = \mathbb{J}(\Omega, T) + \eta(\varepsilon)|\mathcal{B}|\mathbb{T}(\boldsymbol{z}, T) + o(\eta(\varepsilon)) \qquad (\varepsilon \to 0) \tag{7}$$

where the function $\eta(\varepsilon)$, to be determined, vanishes in the limit $\varepsilon \to 0$ and the *topological sensitivity* $\mathbb{T}(\boldsymbol{z}, T)$ is a function of the sampling point $\boldsymbol{z}$ and duration T.

To evaluate the expansion (7) and find the value of $\mathbb{T}(\boldsymbol{z}, T)$, it is necessary to consider the asymptotic behavior of the displacement $\boldsymbol{u}_\varepsilon$ governed by problem $\mathcal{P}(B_\varepsilon(\boldsymbol{z}))$. Towards that aim, it is convenient to decompose $\boldsymbol{u}_\varepsilon$ as

$$\boldsymbol{u}_\varepsilon(\boldsymbol{\xi}, t) = \boldsymbol{u}(\boldsymbol{\xi}, t) + \boldsymbol{v}^\varepsilon(\boldsymbol{\xi}, t) \tag{8}$$

where the free field $\boldsymbol{u}$ is the response of the cavity-free domain Ω to the prescribed excitation, i.e.

$$\mathcal{P}(\emptyset) : \begin{cases} \big[\mathcal{L}\boldsymbol{u}\big](\boldsymbol{\xi}, t) = \boldsymbol{0} & (\boldsymbol{\xi} \in \Omega, t \geqslant 0) \\ \boldsymbol{t}[\boldsymbol{u}](\boldsymbol{\xi}, t) = \bar{\boldsymbol{t}}(\boldsymbol{\xi}, t) & (\boldsymbol{\xi} \in S_{\mathrm{N}}, t \geqslant 0) \\ \boldsymbol{u}(\boldsymbol{\xi}, t) = \bar{\boldsymbol{u}}(\boldsymbol{\xi}, t) & (\boldsymbol{\xi} \in S_{\mathrm{D}}, t \geqslant 0) \\ \boldsymbol{u}(\boldsymbol{\xi}, 0) = \dot{\boldsymbol{u}}(\boldsymbol{\xi}, 0) = \boldsymbol{0} & (\boldsymbol{\xi} \in \Omega) \end{cases} \tag{9}$$

while the scattered field $\boldsymbol{v}^\varepsilon$ solves

$$\begin{cases} \big[\mathcal{L}\boldsymbol{v}^\varepsilon\big](\boldsymbol{\xi}, t) = \boldsymbol{0} & (\boldsymbol{\xi} \in \Omega, t \geqslant 0) \\ \boldsymbol{t}[\boldsymbol{v}^\varepsilon](\boldsymbol{\xi}, t) = -\boldsymbol{t}[\boldsymbol{u}](\boldsymbol{\xi}, t) & (\boldsymbol{\xi} \in \Gamma_\varepsilon(\boldsymbol{z}), t \geqslant 0) \\ \boldsymbol{t}[\boldsymbol{v}^\varepsilon](\boldsymbol{\xi}, t) = \boldsymbol{0} & (\boldsymbol{\xi} \in S_{\mathrm{N}}, t \geqslant 0) \\ \boldsymbol{v}^\varepsilon(\boldsymbol{\xi}, t) = \boldsymbol{0} & (\boldsymbol{\xi} \in S_{\mathrm{D}}, t \geqslant 0) \\ \boldsymbol{v}^\varepsilon(\boldsymbol{\xi}, 0) = \dot{\boldsymbol{v}}^\varepsilon(\boldsymbol{\xi}, 0) = \boldsymbol{0} & (\boldsymbol{\xi} \in \Omega), \end{cases} \tag{10}$$

with $\Gamma_\varepsilon(\boldsymbol{z})$ denoting the boundary of $B_\varepsilon(\boldsymbol{z})$. Since the scattered field is expected to vanish for infinitesimal cavities, i.e. $\|\boldsymbol{v}^\varepsilon(\boldsymbol{\xi}, t)\| = o(\varepsilon)$, expansion (7) is sought by invoking the first-order Taylor expansion of φ w.r.t. to its first argument. The topological sensitivity $\mathbb{T}(\boldsymbol{z}, T)$ and the leading asymptotic behaviour $\eta(\varepsilon)$ are thus to be identified on the basis of:

$$\int_0^T \int_{S^{\mathrm{obs}}} \frac{\partial \varphi}{\partial \boldsymbol{u}}[\boldsymbol{u}(\boldsymbol{\xi}, t), \boldsymbol{\xi}, t]\boldsymbol{v}^\varepsilon(\boldsymbol{\xi}, t)\, \mathrm{d}S_\xi\, \mathrm{d}t = \eta(\varepsilon)|\mathcal{B}|\mathbb{T}(\boldsymbol{z}, T) + o\big(\eta(\varepsilon)\big) \tag{11}$$

In what follows, emphasis will be given to the 3-D case.

3.2 Leading contribution of $\boldsymbol{v}^\varepsilon$ as $\varepsilon \to 0$

To address this issue, it is convenient to reformulate the governing boundary-initial problem (10) in terms of an integral equation. Let $\boldsymbol{U}(\boldsymbol{x}, t, \boldsymbol{\xi})$ and $\boldsymbol{T}(\boldsymbol{x}, t, \boldsymbol{\xi}; \boldsymbol{n})$ denote the time-impulsive elastodynamic Green's tensors, defined such that $\boldsymbol{e}_k \cdot \boldsymbol{U}(\boldsymbol{x}, t, \boldsymbol{\xi})$ and $\boldsymbol{e}_k \cdot \boldsymbol{T}(\boldsymbol{x}, t, \boldsymbol{\xi})$ are the displacement and traction vectors at $\boldsymbol{\xi} \in \Omega$ resulting from a unit time-impulsive point force acting at $\boldsymbol{x}$ in the k-th direction at time $t = 0$ and satisfying the boundary conditions

$$\boldsymbol{U}(\boldsymbol{x}, t, \boldsymbol{\xi}) = \boldsymbol{0} \ \ (\boldsymbol{\xi} \in S_{\mathrm{D}}, t \geqslant 0), \qquad \boldsymbol{T}(\boldsymbol{x}, t, \boldsymbol{\xi}; \boldsymbol{n}) = \boldsymbol{0} \ \ (\boldsymbol{\xi} \in S_{\mathrm{N}}, t \geqslant 0), \tag{12}$$

One also defines the elastodynamic *full-space* fundamental tensors $\boldsymbol{U}_\infty(\boldsymbol{x}, t, \boldsymbol{\xi})$ and $\boldsymbol{T}_\infty(\boldsymbol{x}, t, \boldsymbol{\xi}; \boldsymbol{n})$ in a similar way, replacing boundary conditions (12) with decay and radiation conditions at infinity (Eringen and Suhubi, 1975, see Appendix A.2). The governing integral equation for the scattered field $\boldsymbol{v}^\varepsilon$ then reads (see Appendix A.1)

$$\frac{1}{2}\boldsymbol{v}^\varepsilon(\boldsymbol{x}, t) + \fint_{\Gamma_\varepsilon(z)} \boldsymbol{T}(\boldsymbol{x}, t, \boldsymbol{\xi}; \boldsymbol{n}) \star \boldsymbol{v}^\varepsilon(\boldsymbol{\xi}, t)\, \mathrm{d}S_\xi = -\int_{\Gamma_\varepsilon(z)} \boldsymbol{U}(\boldsymbol{x}, t, \boldsymbol{\xi}) \star \boldsymbol{t}(\boldsymbol{\xi}, t)\, \mathrm{d}S_\xi \qquad (\boldsymbol{x} \in \Gamma_\varepsilon(\boldsymbol{z}),\ t \geqslant 0), \tag{13}$$

in which $\fint$ indicates a (strongly singular) integral defined in the Cauchy principal value (CPV) sense and $\star$ denotes the time convolution at instant $t \geqslant 0$ defined by

$$[\boldsymbol{a} \star \boldsymbol{b}](\boldsymbol{\xi}, t) = \int_0^t \boldsymbol{a}(\boldsymbol{\xi}, \tau) \cdot \boldsymbol{b}(\boldsymbol{\xi}, t-\tau)\, \mathrm{d}\tau. \tag{14}$$

where the inner product appearing in the integral is such that $\boldsymbol{a} \cdot \boldsymbol{b}$ is a tensor of the lowest possible order (e.g. $\boldsymbol{U} \star \boldsymbol{t}$ has order 1, $\boldsymbol{\nabla u} \star \boldsymbol{\sigma}[\boldsymbol{v}]$ is a scalar), and generic tensor fields $\boldsymbol{a}$ and $\boldsymbol{b}$ respectively verify initial and final conditions

$$\boldsymbol{a}(\cdot, \tau) = \dot{\boldsymbol{a}}(\cdot, \tau) = \boldsymbol{0} \ \ (\tau \leqslant 0), \qquad \boldsymbol{b}(\cdot, \tau) = \dot{\boldsymbol{b}}(\cdot, \tau) = \boldsymbol{0} \ \ (\tau \geqslant t) \tag{15}$$

Equations governing the leading contribution of $\boldsymbol{v}^\varepsilon$ on $\Gamma_\varepsilon(\boldsymbol{z})$ as $\varepsilon \to 0$ are sought as the asymptotic form of integral equation (13). For this purpose, scaled coordinates $\bar{\boldsymbol{x}}$ or$\bar{\boldsymbol{\xi}}$, defined by

$$\bar{\boldsymbol{x}} = (\boldsymbol{x} - \boldsymbol{z})/\varepsilon, \quad \bar{\boldsymbol{\xi}} = (\boldsymbol{\xi} - \boldsymbol{z})/\varepsilon \qquad (\boldsymbol{x}, \boldsymbol{\xi} \in \Gamma_\varepsilon(\boldsymbol{z});\ \bar{\boldsymbol{x}}, \bar{\boldsymbol{\xi}} \in \mathcal{S}) \tag{16}$$

are introduced. Consequently, the volume and surface differential elements in $\boldsymbol{\xi}$-space are rescaled according to

$$\text{(a)}\ \ \mathrm{d}V_\xi = \varepsilon^3\, \mathrm{d}\bar{V}_{\bar{\xi}}, \qquad \text{(b)}\ \ \mathrm{d}S_\xi = \varepsilon^2\, \mathrm{d}\bar{S}_{\bar{\xi}} \qquad (\boldsymbol{\xi} \in \Gamma_\varepsilon(\boldsymbol{z}), \bar{\boldsymbol{\xi}} \in \mathcal{S}) \tag{17}$$

where $\mathrm{d}\bar{V}_{\bar{\xi}}$, $\mathrm{d}\bar{S}_{\bar{\xi}}$ denote corresponding volume and surface differential elements on $\mathcal{B}$ and $\mathcal{S}$, respectively. The leading behavior as $\varepsilon \to 0$ of the right- and left-hand sides of integral equation (13) are then given by the following Lemmas 1 and 2, whose proof is given in Appendix A.2.

Lemma 1. *Assume that $\tau \mapsto \boldsymbol{\nabla u}(\boldsymbol{\xi}, \tau)$ is Lipschitz-continuous (uniformly for $\boldsymbol{\xi}$ in a neighbourhood of $\boldsymbol{z}$) and differentiable in a neighbourhood of $\tau = t$. Then, one has*

$$\int_{\Gamma_\varepsilon(z)} \boldsymbol{U}(\boldsymbol{x}, t, \boldsymbol{\xi}) \star \boldsymbol{t}(\boldsymbol{\xi}, t)\, dS_\xi = \varepsilon \left\{ \int_{\mathcal{S}} \boldsymbol{U}_\infty(\bar{\boldsymbol{x}}, \bar{\boldsymbol{\xi}}) \otimes \boldsymbol{n}(\bar{\boldsymbol{\xi}})\, d\bar{V}_{\bar{\xi}} \right\} : \boldsymbol{\sigma}[\boldsymbol{u}](\boldsymbol{z}, t) + o(\varepsilon) \quad (\boldsymbol{x} \in \Gamma_\varepsilon(\boldsymbol{z})) \tag{18}$$

where $\boldsymbol{U}_\infty(\bar{\boldsymbol{x}}, \bar{\boldsymbol{\xi}})$ is the elastostatic *full-space (Kelvin) fundamental displacement, given by (A.12).*

Lemma 2. *Let the vector function $\bar{\boldsymbol{v}}^\varepsilon(\bar{\boldsymbol{\xi}}, t)$ be defined by $\bar{\boldsymbol{v}}^\varepsilon(\bar{\boldsymbol{\xi}}, t) = \boldsymbol{v}^\varepsilon(\boldsymbol{\xi}, t)$, with $\bar{\boldsymbol{\xi}}$ and $\boldsymbol{\xi}$ related through (16). Then, one has*

$$\fint_{\Gamma_\varepsilon(z)} \boldsymbol{T}(\boldsymbol{x}, t, \boldsymbol{\xi}; \boldsymbol{n}) \star \boldsymbol{v}^\varepsilon(\boldsymbol{\xi}, t)\, dS_\xi = \fint_{\mathcal{S}} \boldsymbol{T}_{\infty,\varepsilon}(\bar{\boldsymbol{x}}, t, \bar{\boldsymbol{\xi}}; \boldsymbol{n}) \star \bar{\boldsymbol{v}}^\varepsilon(\bar{\boldsymbol{\xi}}, t)\, d\bar{S}_{\bar{\xi}} + o(\|\bar{\boldsymbol{v}}^\varepsilon(\cdot, t)\|) \quad (\boldsymbol{x} \in \Gamma_\varepsilon(\boldsymbol{z})) \tag{19}$$

where $\boldsymbol{T}_{\infty,\varepsilon}$ is the full-space *elastodynamic fundamental traction tensor defined in terms of rescaled wave velocities c_L/ε, c_T/ε and $\|\bar{\boldsymbol{v}}^\varepsilon(\cdot, t)\|$ is a norm of $\bar{\boldsymbol{\xi}} \mapsto \bar{\boldsymbol{v}}^\varepsilon(\bar{\boldsymbol{\xi}}, t)$, e.g. its L^2-norm on $\mathcal{S}$.*

Lemma 1 means that the leading contribution to the right-hand side of integral equation (13) as $\varepsilon \to 0$ has a special structure wherein the time variable t and the (normalized) space variable $\bar{\boldsymbol{x}}$ are separated. Lemma 2 indicates that the left-hand side of integral equation (13) is of order $O(\|\boldsymbol{v}^\varepsilon\|)$ as $\varepsilon \to 0$. Lemmas 1 and 2 together thus suggest to seek the leading contribution to$\bar{\boldsymbol{v}}^\varepsilon(\bar{\boldsymbol{\xi}}, \tau) = \boldsymbol{v}^\varepsilon(\boldsymbol{\xi}, \tau)$ as $\varepsilon \to 0$ in the following form, in which the third-order tensor function$\bar{\boldsymbol{\xi}} \in \mathcal{S} \mapsto \boldsymbol{\mathcal{V}}(\bar{\boldsymbol{\xi}})$ is to be determined:

$$\bar{\boldsymbol{v}}^\varepsilon(\bar{\boldsymbol{\xi}}, t) = \varepsilon \boldsymbol{\mathcal{V}}(\bar{\boldsymbol{\xi}}) : \boldsymbol{\sigma}[\boldsymbol{u}](\boldsymbol{z}, t) + o(\varepsilon) \quad (\boldsymbol{\xi} \in \Gamma_\varepsilon(\boldsymbol{z}), \bar{\boldsymbol{\xi}} \in \mathcal{S}). \tag{20}$$

Lemma 3. *Let $\bar{\boldsymbol{v}}^\varepsilon(\bar{\boldsymbol{\xi}}, t)$ be of form (20) for some $\boldsymbol{\mathcal{V}}(\bar{\boldsymbol{\xi}})$. Under the assumptions of Lemma 1, one has*

$$\fint_{\Gamma_\varepsilon(z)} \boldsymbol{T}(\boldsymbol{x}, t, \boldsymbol{\xi}; \boldsymbol{n}) \star \boldsymbol{v}^\varepsilon(\boldsymbol{\xi}, t)\, dS_\xi = \varepsilon \left\{ \fint_{\mathcal{S}} \boldsymbol{T}_\infty(\bar{\boldsymbol{x}}, \bar{\boldsymbol{\xi}}; \boldsymbol{n}) \cdot \boldsymbol{\mathcal{V}}(\bar{\boldsymbol{\xi}})\, d\bar{S}_{\bar{\xi}} \right\} : \boldsymbol{\sigma}[\boldsymbol{u}](\boldsymbol{z}, t) + o(\varepsilon) \quad (\boldsymbol{x} \in \Gamma_\varepsilon(\boldsymbol{z})) \tag{21}$$

where $\boldsymbol{T}_\infty(\bar{\boldsymbol{x}}, \bar{\boldsymbol{\xi}}; \boldsymbol{n})$ is the traction associated with the elastostatic Kelvin solution, given by (A.22).

Proof. See Appendix A.2. □

Combining lemmas 1 and 3, one finds that representation (20) indeed holds provided that $\boldsymbol{\mathcal{V}}$ solves the integral equation

$$\frac{1}{2}\boldsymbol{\mathcal{V}}(\bar{\boldsymbol{x}}) + \fint_{\mathcal{S}} \boldsymbol{T}_\infty(\bar{\boldsymbol{x}},\bar{\boldsymbol{\xi}};\boldsymbol{n})\cdot\boldsymbol{\mathcal{V}}(\bar{\boldsymbol{\xi}})\,\mathrm{d}\bar{S}_{\bar{\xi}} = -\int_{\mathcal{S}} \boldsymbol{U}_\infty(\bar{\boldsymbol{x}},\bar{\boldsymbol{\xi}})\otimes\boldsymbol{n}(\bar{\boldsymbol{\xi}})\,\mathrm{d}\bar{S}_{\bar{\xi}} \qquad (\bar{\boldsymbol{x}}\in\mathcal{S}) \tag{22}$$

Upon inspection, (22) can in fact be interpreted as an integral equation formulation governing the solutions $\boldsymbol{\mathcal{V}}_{k\ell} = \boldsymbol{\mathcal{V}}_{\ell k} = (\boldsymbol{e}_k\otimes\boldsymbol{e}_\ell)\!:\!\boldsymbol{\mathcal{V}}$ to a set of six canonical *elastostatic* exterior problems

$$\begin{aligned} &\boldsymbol{\nabla}_{\bar{\xi}}\cdot(\boldsymbol{\mathcal{C}}\!:\!\boldsymbol{\nabla}_{\bar{\xi}}\boldsymbol{\mathcal{V}}_{k\ell})(\bar{\boldsymbol{\xi}}) = \boldsymbol{0} && (\bar{\boldsymbol{\xi}}\in\mathbb{R}^3\setminus\mathcal{B}),\\ &(\boldsymbol{\mathcal{C}}\!:\!\boldsymbol{\nabla}_{\bar{\xi}}\boldsymbol{\mathcal{V}}_{k\ell})(\bar{\boldsymbol{\xi}})\cdot\boldsymbol{n}(\bar{\boldsymbol{\xi}}) = -\frac{1}{2}(n_k(\bar{\boldsymbol{\xi}})\boldsymbol{e}_\ell + n_\ell(\bar{\boldsymbol{\xi}})\boldsymbol{e}_k) && (\bar{\boldsymbol{\xi}}\in\mathcal{S}) \end{aligned} \qquad 1\leqslant k\leqslant\ell\leqslant 3 \tag{23}$$

which are independent of $\boldsymbol{z}$, ε and time. The tensor function $\boldsymbol{\mathcal{V}}(\bar{\boldsymbol{\xi}})$ is in fact completely defined, through problems (23), by $\mathcal{B}$.

The scattered field $\boldsymbol{v}^\varepsilon$ at any point of S^{obs} (and more generally at any point away from the trial cavity $B_\varepsilon(\boldsymbol{z})$) is given by the integral representation formula (see Appendix A.1):

$$\begin{aligned} \boldsymbol{v}^\varepsilon(\boldsymbol{x},t) = \int_{B_\varepsilon(z)} \Big\{\rho\boldsymbol{U}(\boldsymbol{x},t,\boldsymbol{\xi})\star\ddot{\boldsymbol{u}}(\boldsymbol{\xi},t) + \boldsymbol{E}(\boldsymbol{x},t,\boldsymbol{\xi})\star\boldsymbol{\sigma}(\boldsymbol{\xi},t)\Big\}\,\mathrm{d}V_\xi \\ - \int_{\Gamma_\varepsilon(z)} \boldsymbol{T}^k(\boldsymbol{x},t,\boldsymbol{\xi};\boldsymbol{n})\star\boldsymbol{v}^\varepsilon(\boldsymbol{\xi},t)\,\mathrm{d}S_\xi \qquad (\boldsymbol{x}\in S^{\text{obs}},\ t\geqslant 0), \end{aligned} \tag{24}$$

where $\boldsymbol{E}(\boldsymbol{x},t,\boldsymbol{\xi})$ denotes the strain associated with $\boldsymbol{U}(\boldsymbol{x},t,\boldsymbol{\xi})$. Expanding the first integral by means of (17a) and a Taylor expansion of the densities about $\boldsymbol{\xi}=\boldsymbol{z}$, substituting (20) and introducing scaled coordinates $\bar{\boldsymbol{\xi}}$ into the second integral, one obtains the leading contribution of $\boldsymbol{v}^\varepsilon$ as $\varepsilon\to 0$ as:

$$\boldsymbol{v}^\varepsilon(\boldsymbol{x},t) = \varepsilon^3\boldsymbol{W}(\boldsymbol{x},t;\boldsymbol{z}) + o(\varepsilon^3) \tag{25}$$

with

$$\boldsymbol{W}(\boldsymbol{x},t;\boldsymbol{z}) = |\mathcal{B}|\big\{\,[\boldsymbol{\mathcal{C}}\!:\!\boldsymbol{E}(\boldsymbol{x},t,\boldsymbol{z})]\star[\boldsymbol{\mathcal{A}}\!:\!\boldsymbol{\sigma}](\boldsymbol{z},t) + \rho\dot{\boldsymbol{U}}(\boldsymbol{x},t,\boldsymbol{z})\star\dot{\boldsymbol{u}}(\boldsymbol{z},t)\,\big\} \tag{26}$$

and where the constant *polarization tensor* $\boldsymbol{\mathcal{A}}$ depends only on $\mathcal{B}$ (through $\boldsymbol{\mathcal{V}}$) and is defined by

$$\boldsymbol{\mathcal{A}} = \boldsymbol{\mathcal{C}}^{-1} - \frac{1}{|\mathcal{B}|}\Big\{\int_{\mathcal{S}} \boldsymbol{n}(\bar{\boldsymbol{\xi}})\otimes\boldsymbol{\mathcal{V}}(\bar{\boldsymbol{\xi}})\,\mathrm{d}\bar{S}_{\bar{\xi}}\Big\} \tag{27}$$

Inserting (25) into (11), the TS $\mathbb{T}(\boldsymbol{z},t)$ and leading behavior $\eta(\varepsilon)$ are then found to be given by

$$\mathbb{T}(\boldsymbol{z},T) = \int_0^T\int_{S^{\text{obs}}} \frac{\partial\varphi}{\partial\boldsymbol{u}}[\boldsymbol{u}(\boldsymbol{\xi},t),\boldsymbol{\xi},t]\cdot\boldsymbol{W}(\boldsymbol{\xi},t;\boldsymbol{z})\,\mathrm{d}S_\xi\,\mathrm{d}t, \qquad \eta(\varepsilon)=\varepsilon^3 \tag{28}$$

Expression (28) provides a useful basis for discussing some of the features of the time-domain TS, see Sec. 4.1. It can also conceivably be used for the purpose of computing the field $\mathbb{T}(\boldsymbol{z},T)$, and is indeed so used in Chikichev and Guzina (2008) wherein Ω is an elastic half-space with a traction-free surface, a configuration for which the Green's tensor is known. For arbitrary reference bodies Ω, an implementation of (28) would require a numerical evaluation of the Green's tensor for source points located on S^{obs} (typically taken as Gauss quadrature points associated with the evaluation of the integral over S^{obs}) and field points taken as sampling points $\boldsymbol{z}$.

However, a computationally more efficient approach for evaluating the field $\mathbb{T}(\boldsymbol{z},T)$, based on an adjoint solution, is usually preferable and was used for all numerical examples presented thereafter.

3.3 Adjoint field formulation

The adjoint formulation, previously presented in Bonnet (2006) and now summarized for completeness, stems from treating the integral in (11) as one of the terms arising in the elastodynamic reciprocity identity. For any generic domain $\mathcal{O}$ and pair of elastodynamic states $\boldsymbol{u}_1,\boldsymbol{u}_2$ satisfying the

homogeneous elastodynamic field equations in $\mathcal{O}$ as well as homogenous initial conditions

$$\boldsymbol{u}_1(\boldsymbol{\xi},0)=\dot{\boldsymbol{u}}_1(\boldsymbol{\xi},0)=\boldsymbol{0}\quad\text{and}\quad\boldsymbol{u}_2(\boldsymbol{\xi},0)=\dot{\boldsymbol{u}}_2(\boldsymbol{\xi},0)=\boldsymbol{0}\quad(\boldsymbol{\xi}\in\mathcal{O}),$$

the following reciprocity identity holds (see e.g. Eringen and Suhubi, 1975; Achenbach, 2003):

$$\int_{\partial\mathcal{O}}\{\boldsymbol{t}[\boldsymbol{u}_1]\star\boldsymbol{u}_2-\boldsymbol{t}[\boldsymbol{u}_2]\star\boldsymbol{u}_1\}(\boldsymbol{\xi},t)\,\mathrm{d}S_\xi=0 \tag{29}$$

Defining the adjoint state $\hat{\boldsymbol{u}}$ as the solution of:

$$\begin{cases}\big[\mathcal{L}\hat{\boldsymbol{u}}\big](\boldsymbol{\xi},t)=\boldsymbol{0} & (\boldsymbol{\xi}\in\Omega,0\leqslant t\leqslant T)\\ \boldsymbol{t}[\hat{\boldsymbol{u}}](\boldsymbol{\xi},t)=\dfrac{\partial\varphi}{\partial\boldsymbol{u}}[\boldsymbol{u}(\boldsymbol{\xi},T-t),\boldsymbol{\xi},T-t] & (\boldsymbol{\xi}\in S^{\text{obs}},0\leqslant t\leqslant T)\\ \boldsymbol{t}[\hat{\boldsymbol{u}}](\boldsymbol{\xi},t)=\boldsymbol{0} & (\boldsymbol{\xi}\in S_{\text{N}}\backslash S^{\text{obs}},0\leqslant t\leqslant T)\\ \hat{\boldsymbol{u}}(\boldsymbol{\xi},t)=\boldsymbol{0} & (\boldsymbol{\xi}\in S_{\text{D}},0\leqslant t\leqslant T)\\ \hat{\boldsymbol{u}}(\boldsymbol{\xi},0)=\dot{\hat{\boldsymbol{u}}}(\boldsymbol{\xi},0)=\boldsymbol{0} & (\boldsymbol{\xi}\in\Omega)\end{cases} \tag{30}$$

using relation (29) with $\mathcal{V}=\Omega_\varepsilon(\boldsymbol{z})$, $\boldsymbol{u}_1=\hat{\boldsymbol{u}}$ and $\boldsymbol{u}_2=\boldsymbol{v}^\varepsilon$ and exploiting the relevant boundary conditions in (10) and (30), equation (11) becomes:

$$\eta(\varepsilon)|\mathcal{B}|\mathbb{T}(\boldsymbol{z},T)+o\big(\eta(\varepsilon)\big)=-\int_{\Gamma_\varepsilon(z)}\{\boldsymbol{t}[\hat{\boldsymbol{u}}]\star\boldsymbol{v}^\varepsilon\}(\boldsymbol{\xi},t)\,\mathrm{d}S_\xi-\int_{\Gamma_\varepsilon(z)}\{\boldsymbol{t}[\boldsymbol{u}]\star\hat{\boldsymbol{u}}\}(\boldsymbol{\xi},t)\,\mathrm{d}S_\xi \tag{31}$$

On inserting the asymptotic behavior (20) in the first integral, recasting the second integral as a volume integral over $B_\varepsilon(\boldsymbol{z})$ using the divergence identity, and working out the leading contribution as $\varepsilon\to0$ in the resulting equality, one arrives at

$$\mathbb{T}(\boldsymbol{z},T)=\{\boldsymbol{\sigma}[\hat{\boldsymbol{u}}]\star(\boldsymbol{\mathcal{A}}:\boldsymbol{\sigma}[\boldsymbol{u}])+\rho\dot{\hat{\boldsymbol{u}}}\star\dot{\boldsymbol{u}}\}(\boldsymbol{z},T),\qquad\eta(\varepsilon)=\varepsilon^3 \tag{32}$$

where the polarization tensor $\boldsymbol{\mathcal{A}}$ is again defined by (27).

Remark 1. *The $O(\varepsilon^D)$ asymptotic behavior (32) of $\mathbb{J}(\Omega_\varepsilon(\boldsymbol{z}),T)$ relies on $\boldsymbol{v}^\varepsilon$ approaching (up to a scaling factor) a* static *solution as $\varepsilon\to0$. This requires the free-field to be sufficiently regular at $(\boldsymbol{z},t)$, e.g. according to the sufficient condition given in Lemmas 1 and 2. To put this another way, the TS (32) may (invoking the Fourier convolution theorem) be formulated as the inverse Fourier transform of the (previously established in Bonnet and Guzina, 2004) frequency-domain expression*

$$\mathbb{T}(\boldsymbol{z},\omega)=\{\boldsymbol{\sigma}[\hat{\boldsymbol{u}}]:(\boldsymbol{\mathcal{A}}:\boldsymbol{\sigma}[\boldsymbol{u}])-\rho\omega^2\hat{\boldsymbol{u}}\cdot\boldsymbol{u}\}(\boldsymbol{z},\omega)$$

The Fourier integral then converges if $\omega\mapsto\mathbb{T}(\boldsymbol{z},\omega)\in L^1(\mathbb{R})$, i.e. provided the high-frequency content of the excitation is limited. Related considerations are developed in Ammari et al. (2009), where the order in ε of the leading perturbation by a small inclusion of the fundamental solution of the transient wave equation is shown to depend on the high-frequency content of the time-modulated point source.

Remark 2. *In a previous article (Bonnet, 2006), the small-cavity asymptotics was conducted by relying on estimates*

$$\begin{aligned}\boldsymbol{U}(\boldsymbol{x},t,\boldsymbol{\xi})\star\boldsymbol{a}(\boldsymbol{\xi},t)&=\frac{1}{\varepsilon}\boldsymbol{U}_\infty(\bar{\boldsymbol{x}},\bar{\boldsymbol{\xi}})\cdot\boldsymbol{a}(\boldsymbol{z},t)+O(1)\qquad\textit{(a)}\\ \boldsymbol{T}(\boldsymbol{x},t,\boldsymbol{\xi};\boldsymbol{n})\star\boldsymbol{b}(\boldsymbol{\xi},t)&=\frac{1}{\varepsilon^2}\boldsymbol{T}_\infty(\bar{\boldsymbol{x}},\bar{\boldsymbol{\xi}};\boldsymbol{n})\cdot\boldsymbol{b}(\boldsymbol{z},t)+O(1)\quad\textit{(b)}\end{aligned}\qquad(\boldsymbol{x},\boldsymbol{\xi}\in\Gamma_\varepsilon(\boldsymbol{z}))$$

(i.e. identities (27) therein) instead of Lemmas 1 and 2, yielding the same result (32) but in a not entirely correct way: (i) these estimates hold under smoothness conditions on $\boldsymbol{a},\boldsymbol{b}$, similar to the sufficient conditions given in Lemmas 1 and 2, that were not mentioned, and (ii) estimate (b) above is in fact not directly applicable here as it is needed for $\boldsymbol{b}(\boldsymbol{\xi},t)=\boldsymbol{v}^\varepsilon(\boldsymbol{\xi},t)$, which is not defined at $\boldsymbol{\xi}=\boldsymbol{z}$. Lemmas 1 and 2 were therefore needed to fix this flaw in the asymptotic analysis.

Remark 3. *The cavity-identification setting of the model inverse problem formulated in Section 2 is consistent with, but does not constitute a mathematical prerequisite for, the small-cavity asymptotics developed in this section. In fact, the latter procedure may in principle be applied to any cost function of format (5) whatsoever, regardless of its physical meaning or engineering motivation.*

Remark 4. *The same canonical problems (23) and subsequent polarization tensor (27) also occur in Bonnet (2006) and in a previous frequency-domain formulation of the TS (Guzina and Bonnet, 2004).*

Remark 5. *The foregoing analysis has been performed for the 3-D case, deemed the most important, but can be reproduced with the necessary adjustments for the 2-D case (see Appendix A.4), leading to similar results where $\eta(\varepsilon) = \varepsilon^2$ instead of $\eta(\varepsilon) = \varepsilon^3$.*

4 Discussion and implementation

4.1 Discussion

Topological sensitivity as a defect indicator function. $\mathbb{T}(\boldsymbol{z}, T)$ quantifies the sensitivity of the featured cost functional $\mathbb{J}$ to a perturbation of the reference medium in the form of an infinitesimal cavity at $\boldsymbol{z}$. It is then natural to consider $\mathbb{T}(\boldsymbol{z}, T)$ as a possible defect indicator function, as was previously done on several occasions (see Introduction), whereby actual defects are expected to be located at sampling points $\boldsymbol{z}$ at which $\mathbb{T}(\boldsymbol{z}, T)$ attains its most pronounced negative values, i.e. at which a sufficiently small defect would induce the most pronounced decrease of $\mathbb{J}$. In other words, *infinitesimal* trial cavities placed at such sampling points improve the fit between simulated and actual measurements, and intuition then suggests that *finite* defects having the same location also induce a decrease of the cost function. It is important to emphasize that such exploitation of the information provided by the field $\mathbb{T}(\cdot, T)$ is natural but not backed by a rigorous mathematical proof, despite the fact that the analysis of the cost function leading to the definition and evaluation of $\mathbb{T}(\boldsymbol{z}, T)$ is itself mathematically rigorous. It is however substantiated by various numerical experiments performed for several classes of physical settings (see references given in Introduction). The present study aims at contributing to this substantiation within the present context of time-domain elastodynamics, seldom considered in this context, through the examples of Secs. 5 and 6.

Topological sensitivity allows non-iterative approximate global search. Defect identification based on the TS field $\mathbb{T}(\cdot, T)$ of a misfit function has the following important characteristics:

(a) The numerical procedure is non iterative, as it just requires two solutions evaluated on the reference (defect-free) configuration, namely the free field (9) and the adjoint field (30). It is thus computationally much faster than usual iterative optimization-based inversion methods. This non-iterative nature is also one of the main features of the linear sampling method (Arens, 2001; Nintcheu Fata and Guzina, 2007).

(b) The approach is of a qualitative nature, as the underlying approximation (7) of $\mathbb{J}$ does not lend itself to optimization w.r.t. ε.

(c) It is global in nature, as (i) it does not require an initial guess, and (ii) it allows simultaneous identification of multiple defects without prior knowledge of their number (see last example of Sec. 5 and the dual-cavity example in Sec. 6.2).

(d) The experimental information about sought defects entering $\mathbb{T}(\cdot, T)$ is entirely contained in the adjoint solution (through the definition of the adjoint forces in terms of the density φ).

(e) A TS field may be defined and computed using the present approach for cost functions associated to any overdetermined data, no matter how scarce, which makes TS-based identification a very flexible approach.

Transient vs time-harmonic data; time reversal. Compared to previous works based on wave-based imaging under time-harmonic conditions (e.g. Bonnet and Guzina, 2004; Feijóo, 2004; Guzina and Bonnet, 2006; Masmoudi et al., 2005), the time-domain approach to TS benefits from richer data as it exploits measurements taken over a duration T (the mathematical framework allowing to exploit other ways to collect data over time). Dominguez et al. (2005) have compared this approach

to imaging processes based on time reversal (Cassereau et al., 1990), since the adjoint field $\hat{\boldsymbol{u}}$ defined by (30) constitutes a time-reversed state related to the field $\boldsymbol{v}^{\text{true}}$ scattered by the actual defect B^{true}.

Influence of measurement noise. When observed values $\boldsymbol{u}^{\text{obs}}$ differ from their true counterpart $\boldsymbol{u}^{\text{true}}$ because of measurement noise or modelling uncertainties, the sensitivity of $\mathbb{T}(\cdot, T)$ to such uncertainties is directly related to the sensitivity of the adjoint solution to the same uncertainties. In the frequently-used case of least-squares cost functionals, based on (possibly weighted) L^2 norms of measurement residuals $\boldsymbol{\delta} = \boldsymbol{u} - \boldsymbol{u}^{\text{obs}}$, the adjoint forces featured in (30) depend linearly on $\boldsymbol{\delta}$. More generally, misfit functionals based on a L^α norm (with $1 < \alpha < \infty$) lead to $O(\|\boldsymbol{\delta}\|^{\alpha-1})$ adjoint forces (the cases $\alpha = 1, \infty$ do not satisfy the required differentiability of misfit density φ). As $\mathbb{T}(\cdot, T)$ also depends linearly on the adjoint solution (irrespective of the nature of the cost functional), the perturbation undergone by the topological sensitivity of least-squares cost functions is, when using L^2 norms, *linear* in the measurement uncertainties. This suggests that identification procedures based on the TS field are better-behaved with respect to measurement noise than usual inversion procedures, known to be highly sensitive to the latter unless properly regularized. Indeed, numerical results of Sec. 6.5, based on misfit functionals without regularization term, corroborate this expectation.

Dynamical versus static measurements. Expression (28) shows the value of $\mathbb{T}(\boldsymbol{z}, T)$ to be influenced by that of $\boldsymbol{W}(\cdot, \cdot; \boldsymbol{z})$. The latter, defined by (26) in terms of the elastodynamic Green's displacement and strain tensors, is a decreasing function of the distance $d(\boldsymbol{z}, S^{\text{obs}})$ of $\boldsymbol{z}$ to S^{obs}. Hence, sampling points located close to S^{obs} are more apt to lead to high (negative) values of $\mathbb{T}$, increasing the risk of false identifications there when seeking a buried defect. Moreover, it is instructive to compare the behavior of $\mathbb{T}$ for sampling points remote from the observation surface according to whether $\mathbb{T}$ is evaluated under dynamic (i.e. time-dependent) or static (i.e. time-independent) loading conditions. Indeed, $\boldsymbol{W}(\cdot, \cdot; \boldsymbol{z})$ behaves like $[d(\boldsymbol{z}, S^{\text{obs}})]^{-1}$ in the former case, but like $[d(\boldsymbol{z}, S^{\text{obs}})]^{-2}$ in the latter case: (i) this behavior is directly observed for $\boldsymbol{E}(\cdot, \cdot; \boldsymbol{z})$ on the full-space Green's tensor, see Eqs. (A.4ab) and remark 6, and is also explicit for scalar half-space Green's functions, constructed from their full-space counterpart using the method of images; (ii) the second term in (25) vanishes in the time-independent case. The static TS is thus a priori less sensitive than its dynamic counterpart to defects that are remote from the measurement surface.

Computational issues. Anticipating on the finite element implementation discussed next, all numerical results of Secs. 5 and 6 are based on solving *linear* dynamical problems in the time domain, using an unconditionally-stable version of the Newmark time-marching algorithm. Such linear evolution problems have well-established convergence properties with respect to decreasing mesh size and time step, and hence do not raise mesh dependency issues. Note however that discretization error affecting displacement solutions affect quadratically the TS due to the bilinear structure of formula (32). The meshes and time steps used thereafter are chosen solely so as to adequately model geometry and represent expected spatial and time variations in the computed "true", free and adjoint solutions. Also, no attempt to improve the accuracy of computed stresses through refined postprocessing of displacement solutions has been made (although such procedures might conceivably improve TS evaluation), so as to show the usefulness of the TS concept within a standard FEM framework.

4.2 Implementation and numerical experiments

In spite of the previously-mentioned current lack of a mathematical proof to validate rigorously the heuristic idea of a TS-based defect indicator function, it is nevertheless useful to evaluate its practical efficiency through numerical experiments. This study aims at establishing the ability of the time-domain TS to identify defects (here mostly taken as impenetrable objects such as cavities in elastic solids), emphasizing the computational efficiency of the approach and its ease of implementation within a standard finite element framework, and discussing the main features of such wave-based imaging approach. In the sections to follow, results from numerical experiments will be presented for the 2-D scalar wave equation (Section 5), then for 2-D and 3-D elastodynamics (Section 6).

Discretization. Aiming at a FEM-based implementation of the time-domain topological sensitivity of $\mathbb{J}$, let Ω_h and $\Omega_h(B)$ denote FEM discretizations of the reference domain Ω and any cavitated trial domain $\Omega(B)$, whose meshes are assumed to coincide over the (discretized) observation surface S_h^{obs}. Then, a discretized least-squares cost function is be set up in the form

$$\mathbb{J}_h(\Omega_h(B),T) = \sum_{i=1}^{n^{\text{obs}}} \sum_{j=0}^{n_T} \frac{1}{2} \|\boldsymbol{u}_{B,h}(\boldsymbol{\xi}_i,t_j) - \boldsymbol{u}_h^{\text{obs}}(\boldsymbol{\xi}_i,t_j)\|^2 \tag{33}$$

where n^{obs} denote the number of nodes located on S_h^{obs}, $\{t_0=0,\ldots,t_{n_T}=T\}$ is a sequence of discrete time instants (a constant time step Δt being assumed for simplicity), and $\boldsymbol{u}_{B,h},\ \boldsymbol{u}_h^{\text{obs}}$ denote the FE-computed trial displacement and the observed displacement sampled at the nodes of S_h^{obs}, respectively. For the purposes of computing the TS field, it is necessary to set up the discretized reference domain Ω_h, whereas the discretized trial domain $\Omega_h(B)$ is introduced for the purpose of a consistent definition of $\mathbb{J}_h$ but is not actually needed.

In the numerical results to follow, the data $\boldsymbol{u}_h^{\text{obs}}$ is generated synthetically, using a discretized version Ω_h^{true} of the "true" domain with the defects (or set thereof) to be identified. In that case, the meshes of Ω_h^{true} and S_h^{obs} are not required to coincide over S_h^{obs}.

All forward and adjoint solutions are performed using an unconditionally-stable Newmark time-marching scheme with parameters $\beta=1/4, \gamma=1/2$ (Hughes, 1987).

Discretized time convolution. A discrete version of the time convolution (14) is also adopted as

$$[\boldsymbol{v}_h \star \boldsymbol{w}_h](\boldsymbol{\xi}_i,t_k) \approx \Delta t \sum_{j=0}^{k} \boldsymbol{v}_h(\boldsymbol{\xi}_i,t_j)\boldsymbol{w}_h(\boldsymbol{\xi}_i,t_k-t_j) \quad (0 \leqslant k \leqslant n_T). \tag{34}$$

Then the adjoint state $\hat{\boldsymbol{u}}_h$ corresponding to the discretized cost function (33) is defined on Ω_h and results from time-dependent *nodal* forces $\hat{\boldsymbol{F}}_h$ over S_h^{obs} defined by

$$\hat{\boldsymbol{F}}_h(\boldsymbol{\xi}_i,t_j) = \boldsymbol{u}_h(\boldsymbol{\xi}_i,t_T-t_j) - \boldsymbol{u}_h^{\text{obs}}(\boldsymbol{\xi}_i,t_T-t_j) \quad (1 \leqslant i \leqslant n^{\text{obs}},\ 0 \leqslant k \leqslant n_T) \tag{35}$$

Truncated topological sensitivity. To focus on areas of Ω where $\mathbb{T}$ attains sufficiently low (negative) values, a thresholded version $\mathbb{T}_\alpha$ of $\mathbb{T}$ depending on a cut-off parameter α is used in some of the following examples. It is defined by

$$\mathbb{T}_\alpha(\boldsymbol{z},T) = \begin{cases} \mathbb{T}(\boldsymbol{z},T) & (\mathbb{T} \leqslant \alpha \mathbb{T}^{\min}), \\ 0 & (\mathbb{T} > \alpha \mathbb{T}^{\min}) \end{cases} \qquad \text{with } \mathbb{T}^{\min} = \min_{\boldsymbol{z}} \mathbb{T}(\boldsymbol{z},T),\ \alpha<1, \tag{36}$$

with the implicit assumption that $\mathbb{T}^{\min}<0$. Moreover, let $B_{\text{eq}}(\alpha)$ denote the geometrical support of $\mathbb{T}_\alpha(\boldsymbol{z},T)$, i.e. the region of Ω defined by

$$B_{\text{eq}}(\alpha) = \left\{ \boldsymbol{z} \in \Omega \;\middle|\; \mathbb{T}_\alpha(\boldsymbol{z},T) < 0 \right\}. \tag{37}$$

Thus an estimation of the unknown cavity (or set thereof) suggested by the thresholded TS may be defined in terms of $B_{\text{eq}}(\alpha)$. The following additional definitions will also be useful: the characteristic radius $R_{\text{eq}}(\alpha)$ of $B_{\text{eq}}(\alpha)$, given by

$$R_{\text{eq}} = \left(\frac{1}{\pi} |B_{\text{eq}}| \right)^{1/2} \text{(2-D)}, \qquad R_{\text{eq}} = \left(\frac{3}{4\pi} |B_{\text{eq}}| \right)^{1/3} \text{(3-D)}, \tag{38}$$

where $|B_{\text{eq}}|$ stands for the volume of B_{eq}, and the distance $d(\alpha)$ between the centroid $\boldsymbol{x}_{\text{eq}}$ of $B_{\text{eq}}(\alpha)$ and the true cavity centroid $\boldsymbol{x}^{\text{true}} \in \Omega$, i.e.

$$d = |\boldsymbol{x}^{\text{true}} - \boldsymbol{x}_{\text{eq}}| \quad \text{ with } \boldsymbol{x}_{\text{eq}} = \frac{1}{|B_{\text{eq}}|} \int_{B_{\text{eq}}} \boldsymbol{\xi} \, \mathrm{d}V_\xi \tag{39}$$

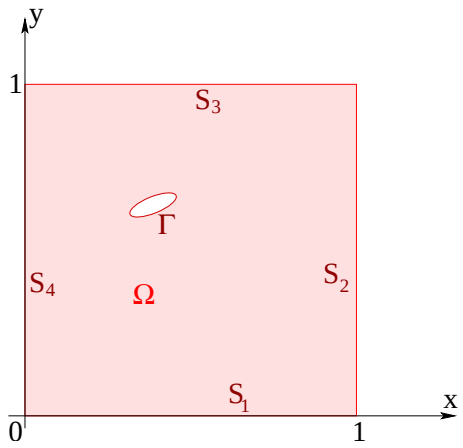

Figure 1: *Defect imaging using acoustic time-domain data: geometry and notations.*

5 Defect imaging using acoustic time-domain data

In this set of examples, the reference domain Ω is the unit square, i.e. $\Omega = \{0 \leqslant \xi_1, \xi_2 \leqslant 1\}$ (Fig. 1). The primary field is governed by the two-dimensional scalar wave equation of e.g. linear acoustics. The identification of a set B^{true} of impenetrable obstacles, such that a homogeneous Neumann boundary condition describing a zero normal velocity is prescribed on the obstacle boundary Γ^{true}, is considered, based on four (simulated) experiments of duration T. The free pressure field $u^{(k)}$ associated to experiment number k is defined through the boundary-initial value problem

$$\begin{aligned} \Delta u^{(k)}(\boldsymbol{\xi},t) - \ddot{u}^{(k)}(\boldsymbol{\xi},t) = 0 \quad & (\boldsymbol{\xi} \in \Omega,\ 0 \leqslant t \leqslant T) \\ \boldsymbol{\nabla} u^{(k)}(\boldsymbol{\xi},t) \cdot \boldsymbol{n}(\boldsymbol{\xi}) = 1 \quad & (\boldsymbol{\xi} \in S_k,\ 0 \leqslant t \leqslant T) \\ \boldsymbol{\nabla} u^{(k)}(\boldsymbol{\xi},t) \cdot \boldsymbol{n}(\boldsymbol{\xi}) = 0 \quad & (\boldsymbol{\xi} \in S_\ell\ (\ell \neq k),\ 0 \leqslant t \leqslant T) \\ u^{(k)}(\boldsymbol{\xi},0) = \dot{u}^{(k)}(\boldsymbol{\xi},0) = 0 \quad & (\boldsymbol{\xi} \in \Omega) \end{aligned} \tag{40}$$

where each S_ℓ is one of the sides of the square boundary of Ω, numbered according to Fig. 1, and Δ denotes the two-dimensional Laplacian operator. Note that the wave velocity is set to $c = 1$, so that the travel time of waves propagating vertically from S_1 to S_3 or horizontally from S_2 to S_4 is one unit of time. All simulations presented in this section were performed using a finite element method based on a piecewise-linear interpolation, i.e. three-noded triangular elements. The cost function

$$J^{(k)}(B,T) = \frac{1}{2} \int_0^T \int_{S_1+S_2+S_3+S_4} |u_B^{(k)}(\boldsymbol{\xi},t) - u_{\text{obs}}^{(k)}(\boldsymbol{\xi},t)|^2 \, \mathrm{d}s_\xi \, \mathrm{d}t$$

is then introduced (in a discretized form similar to (33)), where $u_{\text{true}}^{(k)}$ denotes the pressure field arising in $\Omega^{\text{true}} = \Omega \setminus B^{\text{true}}$ from the external excitation defined in (40), $u_{\text{obs}}^{(k)}$ is the corresponding (possibly polluted) observation, and $u_\Gamma^{(k)}$ is the predicted measurement for an assumed configuration B of the obstacle. The topological sensitivity $\mathbb{T}(\boldsymbol{z},T)$ of $J^{(k)}$, such that

$$J^{(k)}(\Omega_\varepsilon(\boldsymbol{z}),T) = J^{(k)}(\Omega,T) + \varepsilon^2 |\mathcal{B}| \mathbb{T}(\boldsymbol{z},T) + o(\varepsilon^2)$$

is given (following an analysis similar to that of Sec. 3) by

$$\mathbb{T}(\boldsymbol{z},T) = \left\{ 2\pi \boldsymbol{\nabla} u^{(k)} \star \boldsymbol{\nabla} \hat{u}^{(k)} + \frac{4\pi}{3} u^{(k)} \hat{u}^{(k)} \right\}(\boldsymbol{z},t)$$

Identification of a single scatterer. Let B^{true} denote the ellipse with parameters as given for scatterer 1 in Table 1 (where "inclination" refers to the angle between the ξ_1-direction and the major

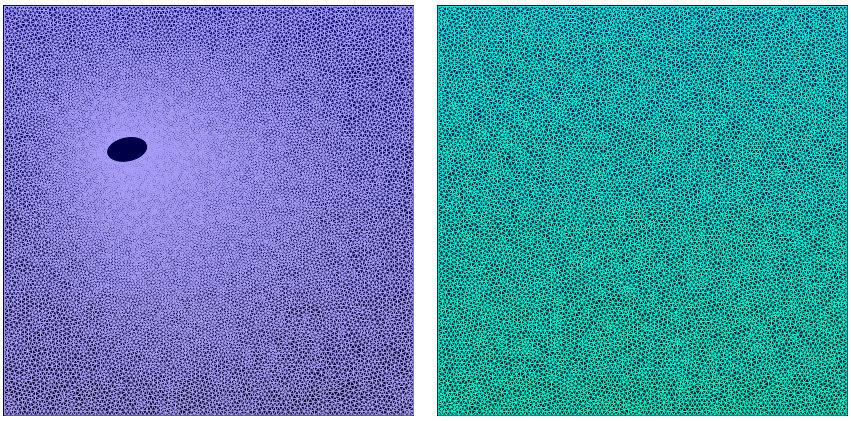

Figure 2: *Identification of a single scatterer: meshes used for generating the synthetic data (left) and computing the topological sensitivity (right).*

principal axis). The meshes used for generating the synthetic data $u_{\text{true}}^{(k)}$ and for computing $u, \hat{u}$ and $\mathbb{T}(\cdot, T)$ (Fig. 2) feature 16 268 and 9 841 DOFs, respectively.

Figure 3 shows the distribution of $\mathbb{T}_\alpha(\cdot, T)$ obtained for the above-defined single-scatterer identification problem (having used $T = 2$, $\alpha = 1/2$ and $\Delta t = 2.5\,10^{-2}$). The region $B_{\text{eq}}(\alpha)$ clearly pinpoints correctly the location of the defect, while its size gives a reasonable estimation of the actual defect size. Figure 4 moreover shows, by means of a sequence of blow-ups of the region surrounding the actual defects for α ranging from 0.1 to 0.9, that $B_{\text{eq}}(\alpha)$ is relatively insensitive to the choice of α within a fairly wide range of values (approximately $0.2 \leqslant \alpha \leqslant 0.6$ for this example).

Figure 5 then illustrates how the choice of experiment configuration and duration affects the results. Figure 5(a), which repeats Fig. 3, is based on the single experiment $k = 1$ and a duration $T = 2$ large enough for a wave emanating from S_1 to hit the defect and send scattered signals back to various parts of the boundary. Hence, the cost function contains enough data about the object to make an identification possible. In contrast, under the same conditions but with data collected only until $T = 1$, the scattering of a wave emanating from S_1 seldom has sufficient time to send information to the boundary, and the defect is not identified (Fig. 5(b)). Using the same reduced experiment duration $T = 1$ but with an incident wave emanating from surface S_4, located closer to the defect, some of the scattered signals reach the boundary before $t = 1$ resulting in an identification (Fig. 5(c)) that is not as good as in Fig. 5(a) but still acceptable. Finally, maintaining $T = 1$ and using a multiple experiment $k = 1, 2, 3, 4$ (with experiments $k = 3, 4$ contributing most of the usable data due to the chosen duration) yields again a satisfactory identification (Fig. 5(d)). These observations entirely conform with what one would expect based on physical intuition.

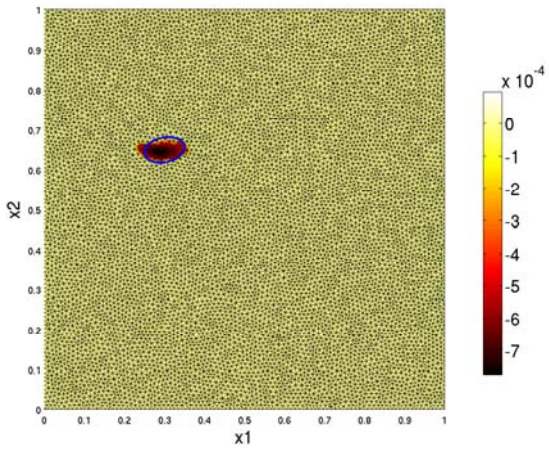

Figure 3: *Identification of a single scatterer: distribution of thresholded topological sensitivity $\mathbb{T}_\alpha$, with $T = 2$ and $\alpha = 1/2$.*

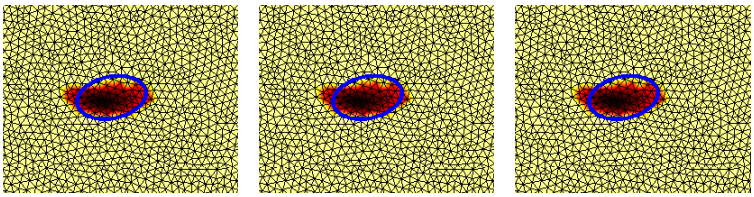

(a) $\alpha = 0.1$ (b) $\alpha = 0.2$ (c) $\alpha = 0.3$

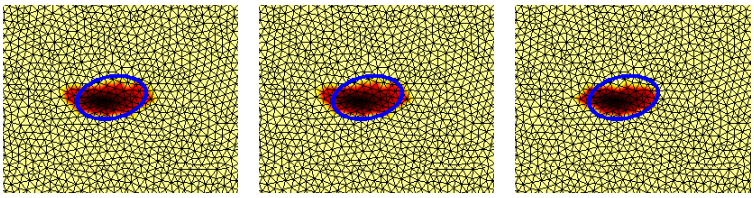

(d) $\alpha = 0.4$ (e) $\alpha = 0.5$ (f) $\alpha = 0.6$

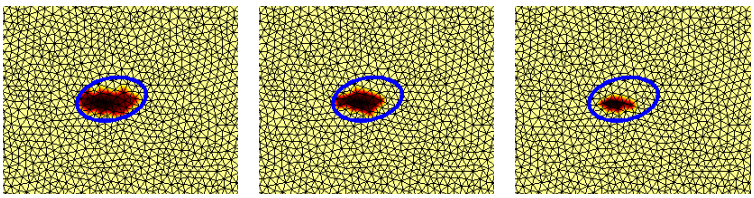

(g) $\alpha = 0.7$ (h) $\alpha = 0.8$ (i) $\alpha = 0.9$

Figure 4: *Identification of a single scatterer: influence of cut-off parameter* α.

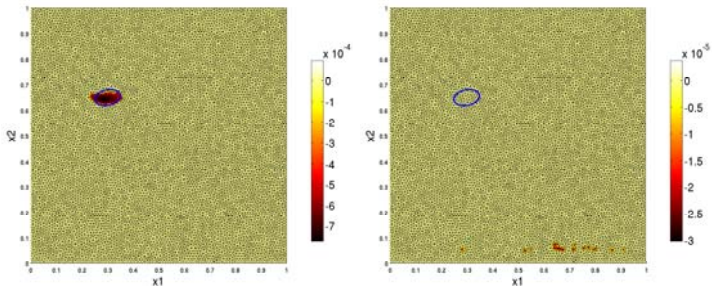

(a) $k = 1,\ T = 2$ (b) $k = 1,\ T = 1$

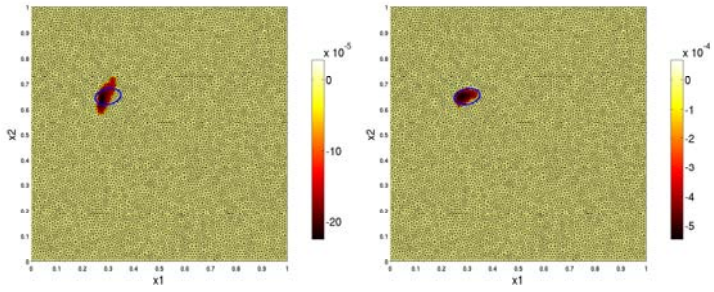

(c) $k = 4,\ T = 1$ (d) $k = 1, 2, 3, 4,\ T = 1$

Figure 5: *Identification of a single scatterer: influence of experiment configuration and duration.*

Simultaneous identification of a multiple scatterer. The simultaneous identification of a set of four elliptical scatterers, whose characteristics are gathered in Table 1, is now considered. The mesh used for generating the synthetic data $u_{\text{true}}^{(k)}$ now features 24 098 DOFs. The resulting distribution of $\mathbb{T}_\alpha(\cdot, T)$ obtained for a multiple simulated experiment $k = 1, 2, 3, 4$ with duration $T = 2$ and a cut-off $\alpha = 0.5$ is shown in Fig. 6. The corresponding region $B_{\text{eq}}(\alpha)$ is split into four connected components, each one correctly located at one of the defects. The identification is simultaneous in that the topological sensitivity is computed at once on the basis of the free and adjoint solutions, with

Scatterer #	Semiaxes	Centroid	Inclination
1	$\sqrt{26}/100,\ 3\sqrt{26}/500$	$(0.30, 0.65)$	$\tan^{-1}(1/5)$
2	$\sqrt{29}/100,\ 3\sqrt{26}/400$	$(0.60, 0.35)$	$\tan^{-1}(5/2)$
3	$\sqrt{17}/100,\ 3\sqrt{17}/200$	$(0.25, 0.30)$	$\tan^{-1}(1/5)$
4	$\sqrt{13}/100,\ 3\sqrt{13}/200$	$(0.55, 0.75)$	$\tan^{-1}(5/2)$

Table 1: *Identification of a multiple scatterer: geometrical parameters.*

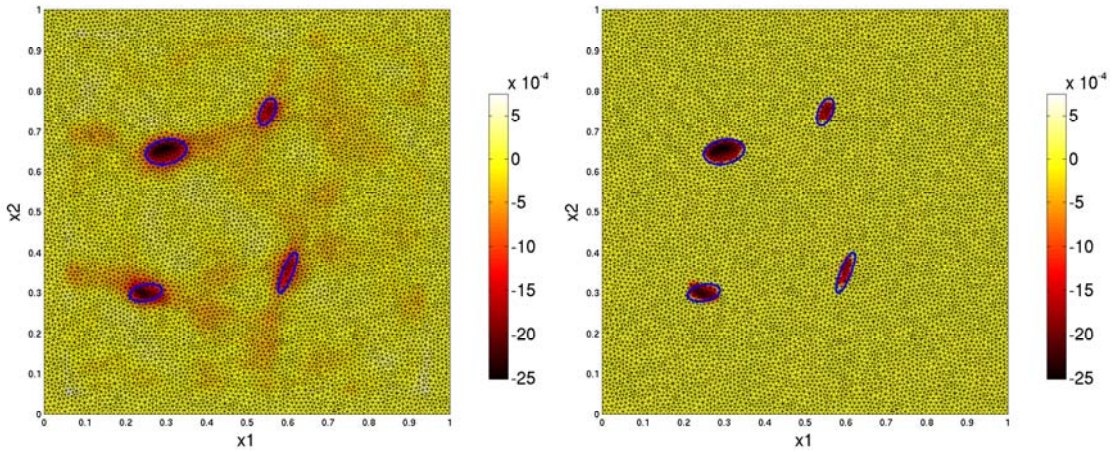

Figure 6: *Identification of a multiple scatterer, with $k = 1, 2, 3, 4$ and $T = 2$: TS field $\mathbb{T}$ (left) and its thresholded version $\mathbb{T}_\alpha$ with $\alpha = 1/2$ (right).*

no prior information about the number of defects fed into the computation.

6 Defect imaging using elastodynamic time-domain data

6.1 Methodology

Synthetic experiment configuration. The reference elastic domains considered are the unit cube $\Omega = \{0 \leqslant \xi_1, \xi_2, \xi_3 \leqslant 1\}$ or the unit square $\Omega = \{0 \leqslant \xi_1, \xi_2 \leqslant 1\}$. The material parameters μ, ν, ρ are set so that the longitudinal wave velocity (which is fastest) is unity:

$$c_{\mathrm{L}} = \sqrt{\mu/\rho\kappa^2} = 1 \tag{41}$$

(with κ defined by (A.5)), so that $T = 1$ corresponds to the travel time of longitudinal waves propagating between any two opposite faces of $\partial\Omega$ in a direction normal to them. For both 3D and 2D cases, a single synthetic experiment is considered throughout this section, whereby a compressional loading $\bar{\boldsymbol{t}} = -H(t)\boldsymbol{e}_2$ (where $H(t)$ denotes the Heaviside step function) is applied on the face $\xi_2 = 1$ of $\partial\Omega$ while a homogenous Dirichlet condition is prescribed on the face $S_{\mathrm{D}} = \{\xi_2 = 0\}$. The observation surface is taken as the whole Neumann surface: $S_h^{\mathrm{obs}} = S_{\mathrm{N}} = \partial\Omega_h \setminus S_{\mathrm{D}}$.

The reference mesh Ω_h is based on an isoparametric piecewise-linear interpolation employing three-noded triangular elements and 1988 nodes (2D case) or four-noded tetrahedral elements and 19683 nodes (3D case). Moreover, to guard against the "inverse crime" (Colton and Kress, 1998), the synthetic data $\boldsymbol{u}^{\mathrm{obs}}$ is computed by means of a finer discretization, with Ω_h^{true} discretized into isoparametric piecewise-quadratic elements, i.e. six-noded triangular elements (2D case) or ten-noded tetrahedral elements (3D case), arranged for convenience so that the elements of Ω_h and Ω_h^{true} coincide on S^{obs}. The simulated displacements at the vertex nodes of Ω_h^{true} on S^{obs} are then retained (and the values at the midside nodes discarded), which provide the nodal values of $\boldsymbol{u}^{\mathrm{obs}}$ on S_h^{obs} used in the discrete cost function (33).

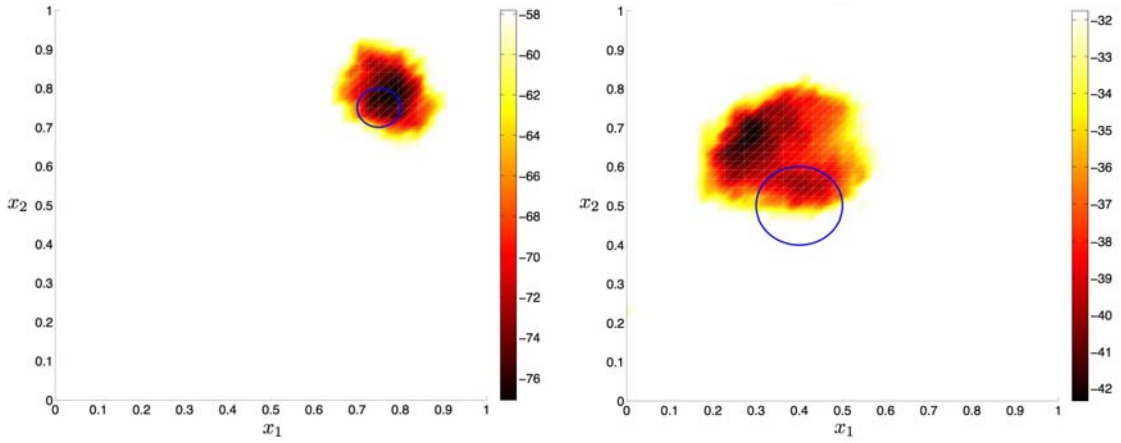

(a) $R_1 = 0.05$, $\boldsymbol{x}^{\text{true}} = (0.75,\ 0.75)$ (b) $R_1 = 0.1$, $\boldsymbol{x}^{\text{true}} = (0.4,\ 0.5)$

Figure 7: *Single cavity identification, 2D: thresholded TS field* $\mathbb{T}_\alpha$ *with* $\alpha = 0.75$.

6.2 Single or dual cavity identification

In this section, the effectiveness of the topological sensitivity indicator is assessed on 2-D or 3-D single- or dual-cavity configurations, with the simulated experiment duration set to $T = 1$.

The thresholded TS $\mathbb{T}_\alpha(\cdot, T)$ for a single unknown circular cavity and a set of two unknown circular cavities are presented, for two configurations in each case, in Figs. 7 and 8, respectively (with details on cavity geometry provided therein). In each figure, case (a) corresponds to unknown cavities close enough to the excitation surface, so that the experiment duration $T = 1$ lets sufficient amount of information reach the observation surface, leading to satisfactory identification for both the single- or dual-cavity cases. In contrast, case (b) for each figure features a cavity located in such a way that little information about its presence can reach the observation surface within the time frame $T = 1$, and these cavities are poorly located by the $\mathbb{T}_\alpha(\cdot, T)$ distribution. In addition, a computation on two finer meshes of the thresholded TS of Fig. 7(a), keeping the same measurement grid and definition (35) of adjoint nodal forces, indicates that $\mathbb{T}_\alpha(\cdot, T)$ is only moderately sensitive to mesh size (Fig. 9).

Then, similar numerical experiments are conducted for the 3-D case, with results for single- or dual-cavity configurations shown in Figs. 10 and 11 (where details on cavity geometry are again provided therein, and the correct cavity boundaries are depicted as blue spheres). Moreover, the regions $B_{\text{eq}}(\alpha)$ defined by (37), plotted respectively in Figs. 12 and 13 for the single- and dual-cavity cases, are seen to indicate the correct location and number of sought cavities based on the sole information $\boldsymbol{u}^{\text{obs}}$ and do not predict other, spurious, defects.

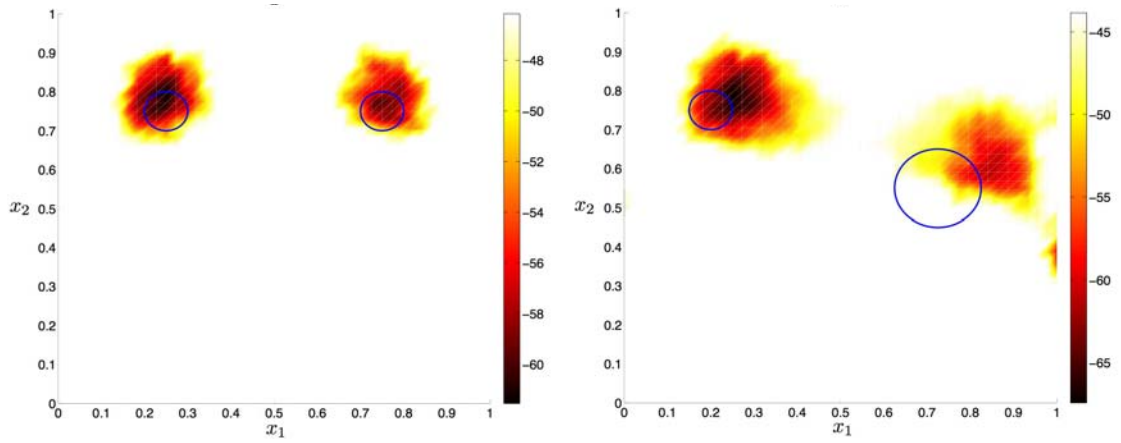

(a) $\alpha = 0.75$, $R_1 = R_2 = 0.05$,
$\boldsymbol{x}_1^{\text{true}} = (0.25,\ 0.75)$, $\boldsymbol{x}_2^{\text{true}} = (0.75,\ 0.75)$

(b) $\alpha = 0.65$, $R_1 = 0.05$, $R_2 = 0.1$,
$\boldsymbol{x}_1^{\text{true}} = (0.2,\ 0.75)$, $\boldsymbol{x}_2^{\text{true}} = (0.75,\ 0.55)$

Figure 8: *Dual cavity identification, 2D: thresholded TS field* $\mathbb{T}_\alpha$.

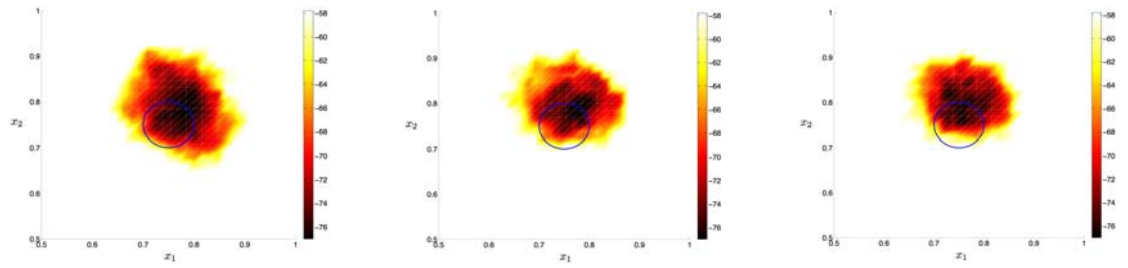

(a) Same mesh as Fig. 7 (1988 nodes) (b) Refined mesh 1 (3027 nodes) (c) Refined mesh 2 (4416 nodes)

Figure 9: *Single cavity identification, 2D ($R_1 = 0.05$, $\boldsymbol{x}^{true} = (0.75,\ 0.75)$): thresholded TS field $\mathbb{T}_\alpha$ with $\alpha = 0.75$ for three different meshes.*

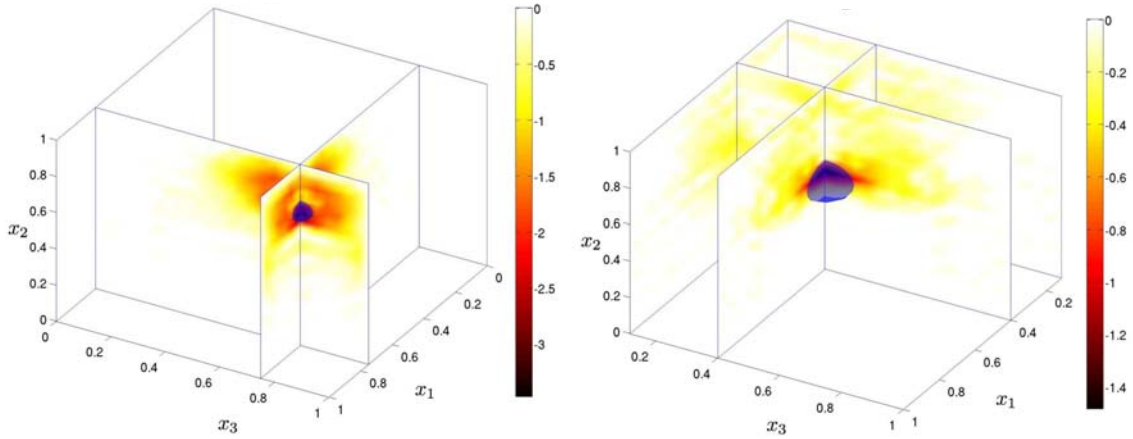

(a) $R = 0.05$, $\boldsymbol{x}^{\text{true}} = (0.75,\ 0.75,\ 0.75)$ (b) $R = 0.1$, $\boldsymbol{x}^{\text{true}} = (0.4,\ 0.4,\ 0.5)$

Figure 10: *Single cavity identification, 3D: thresholded TS field $\mathbb{T}_\alpha$ with $\alpha = 0$.*

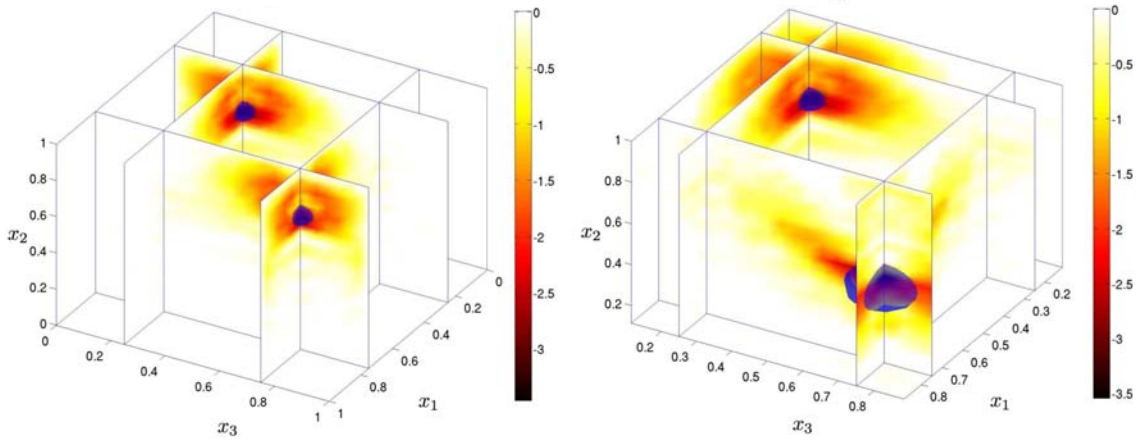

(a) $R_1 = R_2 = 0.05$, $\boldsymbol{x}_1^{\text{true}} = (0.25,\ 0.25,\ 0.75)$, $\boldsymbol{x}_2^{\text{true}} = (0.75,\ 0.75,\ 0.75)$ (b) $R_1 = 0.05 \quad R_2 = 0.1$, $\boldsymbol{x}_1^{\text{true}} = (0.25,\ 0.25,\ 0.75)$, $\boldsymbol{x}_2^{\text{true}} = (0.75,\ 0.75,\ 0.5)$

Figure 11: *Dual cavity identification, 3D: thresholded TS field $\mathbb{T}_\alpha$ with $\alpha = 0$.*

6.3 Influence of experiment duration

The duration T over which data is collected will obviously have a major effect on the results, an effect which is now investigated. For this purpose, in addition to the previously-defined unit cube or square Ω, an elongated variant Ω' of Ω such that $-1 \leqslant \xi_2 \leqslant 1$ is also considered, with $S'_{\text{D}} = \{\xi_2 = -1\}$ and all other dimensions and boundary conditions defined as before, and the corresponding observation surface S'^{obs} set as $S'^{\text{obs}} = S'_{\text{N}} = \partial\Omega' \setminus S'_{\text{D}}$.

Figures 14 and 15 plot $d(0.75)$ and $R_{\text{eq}}(0.75)$ as functions of the simulated experiment duration T for the identification of a single cavity of radius $R = 0.1$ embedded in domain Ω or Ω'. Both the 2-D case (with $\boldsymbol{x}_1^{\text{true}} = (0.5,\ 0.5)$ in Ω or $\boldsymbol{x}_2^{\text{true}} = (-0.5,\ 0.5)$ in Ω') and the 3-D case (with

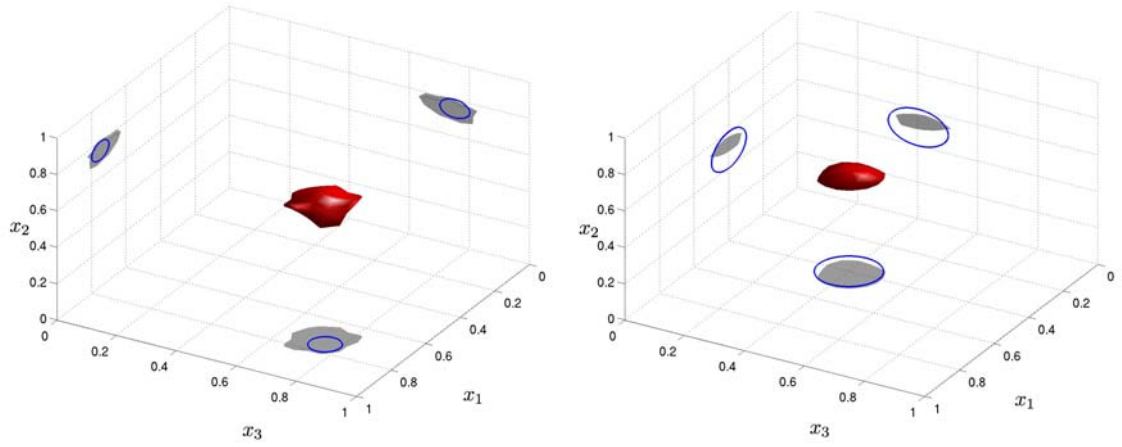

(a) $R = 0.05$, $\alpha = 0.6$ (b) $R = 0.1$, $\alpha = 0.6$

Figure 12: *Single cavity identification, 3D:* $B_{eq}(\alpha)$.

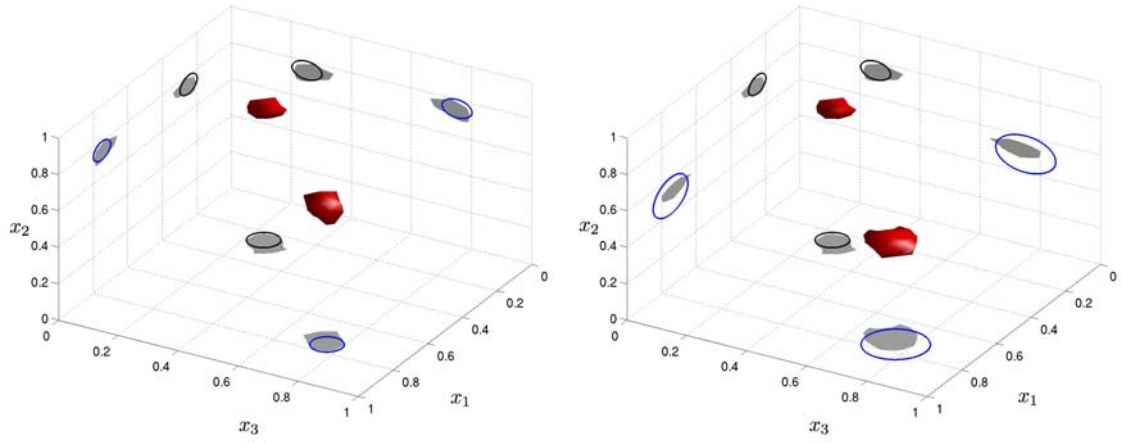

(a) $R_1 = R_2 = 0.05$, $\alpha = 0.6$ (b) $R_1 = 0.05 \quad R_2 = 0.1$, $\alpha = 0.7$

Figure 13: *Dual cavity identification, 3D:* $B_{eq}(\alpha)$.

$\boldsymbol{x}_1^{\text{true}} = (0.5,\, 0.5,\, 0.5)$ in Ω or $\boldsymbol{x}_2^{\text{true}} = (0.5,\, -0.5,\, 0.5)$ in Ω') are considered. These results can be divided into three cases (indicated on Figs. 14 and 15 using circled '1', '2' and '3' symbols) according to the value taken by T. For $0 < T \leqslant T_1$ (where T_1 is typically the time for the wave to reach the cavity), the identification is not satisfactory, as was to be expected since the scattered waves do not have time to reach S^{obs} and be recorded in the cost function. Next, the case $T_1 \leqslant T \leqslant T_2$ (relatively narrow in terms of the range of T) corresponds to d decreasing, and R_{eq} increasing, with T i.e. estimations of defect location and size that are sensitive to the experiment duration (figures 14(b), 15(a), 15(b)) and hence also not reliable. Finally, in the case $T \geqslant T_2$ (with T_2 large enough for a substantial amount of information to reach S^{obs}), d reaches small values (indicating a correct identification of the cavity location) while R_{eq}, the estimated cavity size, attains stable values.

6.4 Influence of observation surface configuration

All results so far were based on dense and full-aperture measurements (for a single experiment). The effect of relaxing either the measurement grid density or the measurement aperture is now considered.

Influence of measurement grid density. The influence of using coarser measurement grids featuring $N \times N$ points on each face of S_{N} is now considered. Figure 16 illustrates the effect of a decreasing measurement density (i.e. decreasing N) on the computed field $\mathbb{T}_\alpha(\cdot, T)$. The numerical value of $\mathbb{T}_\alpha(\cdot, T)$ is seen to decrease, reflecting the fact that the definition (33) of $\mathbb{J}$ and that of the adjoint forces (35) is strongly influenced by the number of measurement points. This in itself is of secondary importance, as (i) the support of $\mathbb{T}_\alpha(\cdot, T)$, not its numerical value, is of primary impor-

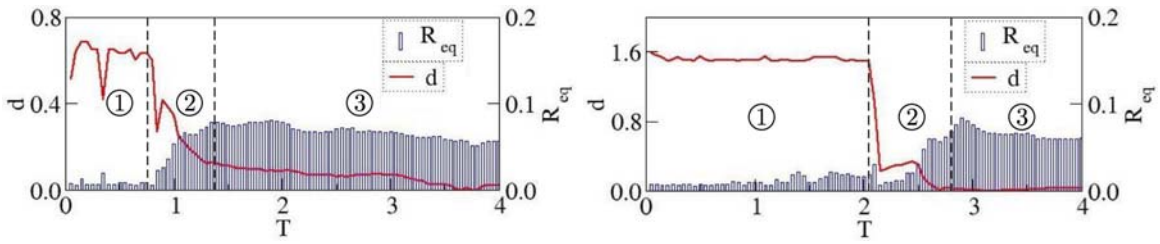

(a) $R = 0.1$, $\boldsymbol{x}_1^{\text{true}} = (0.5,\ 0.5)$ (b) $R = 0.1$, $\boldsymbol{x}_2^{\text{true}} = (0.5,\ -0.5)$

Figure 14: *Influence of experiment duration: identification under 2-D conditions.*

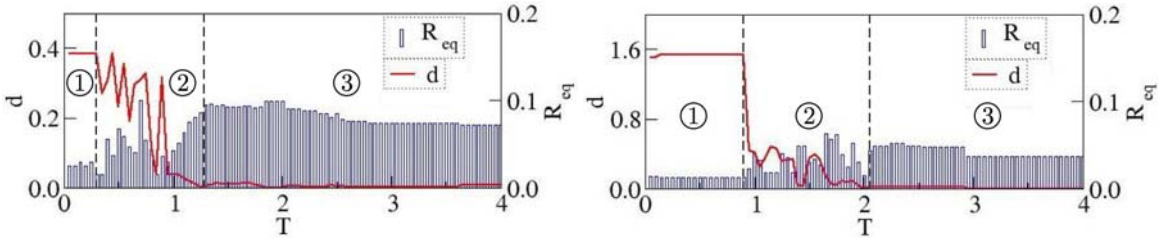

(a) $R = 0.1$, $\boldsymbol{x}_1^{\text{true}} = (0.5,\ 0.5,\ 0.5)$ (b) $R = 0.1$, $\boldsymbol{x}_2^{\text{true}} = (0.5,\ -0.5,\ 0.5)$

Figure 15: *Influence of experiment duration: identification under 3-D conditions.*

tance, and (ii) one could easily renormalize the definition of $\mathbb{J}$. However, one also notices that a decreasing measurement density induces a qualitative deterioration of the identification provided by $\mathbb{T}_\alpha(\cdot, T)$. This observation is confirmed by Fig. 17, where the reconstructed cavity is taken to be the support $B_{\text{eq}}(\alpha)$ of $\mathbb{T}_\alpha(\cdot, T)$ and which shows that α must decrease with N to have $B_{\text{eq}}(\alpha)$ reasonably

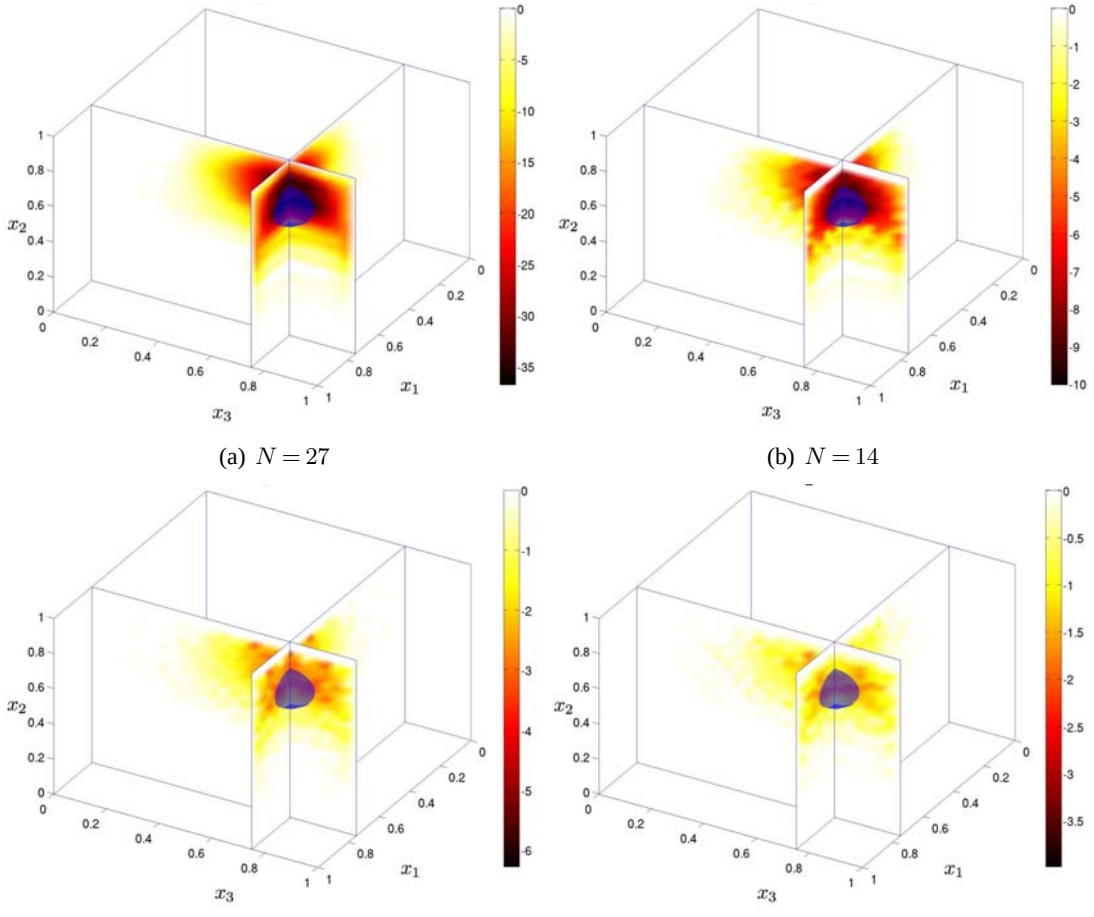

(a) $N = 27$ (b) $N = 14$

(c) $N = 9$ (d) $N = 7$

Figure 16: *Influence of measurement grid density on thresholded TS field* $\mathbb{T}_\alpha$ *(*$\alpha = 0$, $R = 0.1$*)*

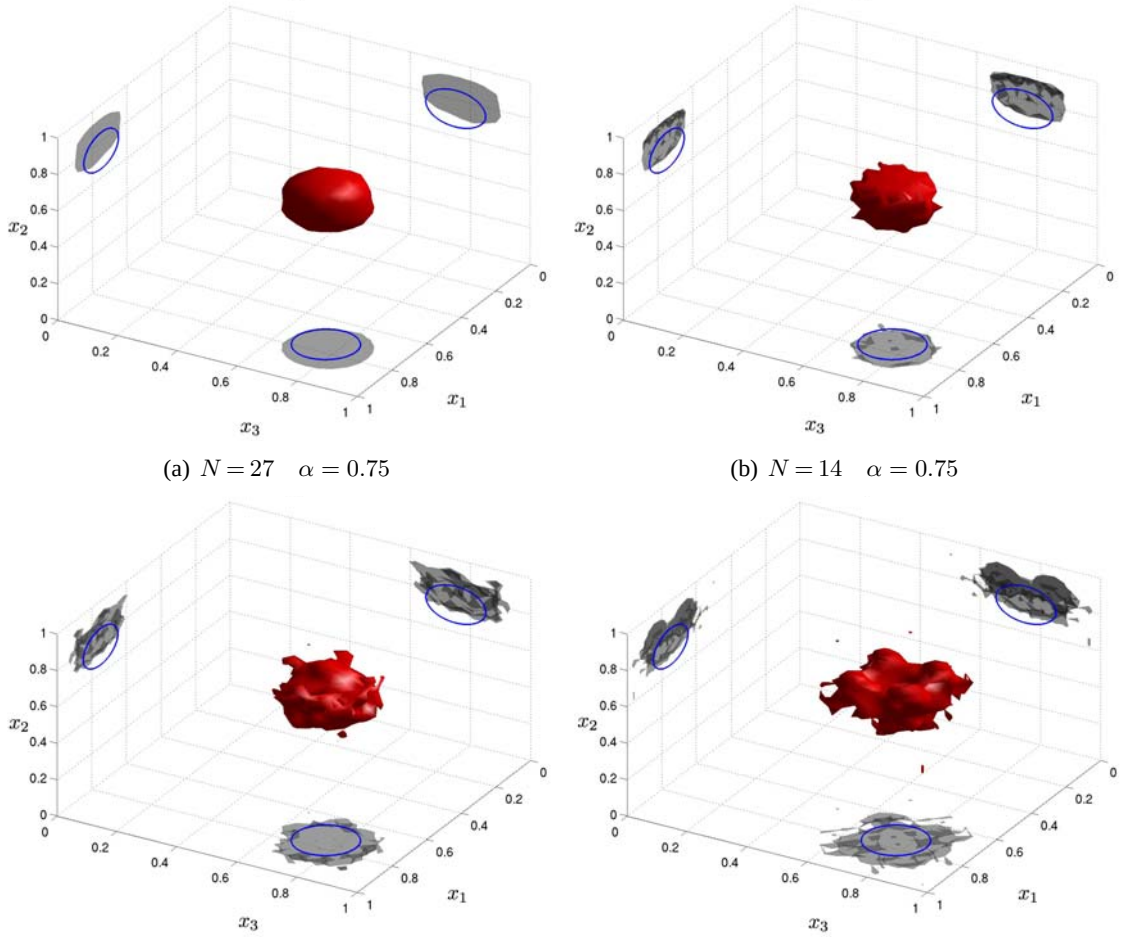

(a) $N = 27 \quad \alpha = 0.75$ (b) $N = 14 \quad \alpha = 0.75$

(c) $N = 9 \quad \alpha = 0.4$ (d) $N = 7 \quad \alpha = 0.35$

Figure 17: *Influence of measurement grid density: blurring effect on* $B_{eq}(\alpha)$.

estimating B^{true} for all grid densities. Remarkably, the cavity location remains correctly estimated even as the shape of $B_{\text{eq}}(\alpha)$ becomes irregular due to the decreasing number of observation points.

Influence of limited aperture. Here, the effect of restricting the observation surface to a portion $S^{\text{obs}} \subsetneq S_{\text{N}}$ of the boundary is examined. Figure 18 shows the identification result in terms of $B_{\text{eq}}(\alpha)$ for two cases with limited aperture. For data collected on the top face $\xi_2 = 1$ (Fig. 18(a)), the observation surface is orthogonal to the propagation direction of the compressional wave in the reference

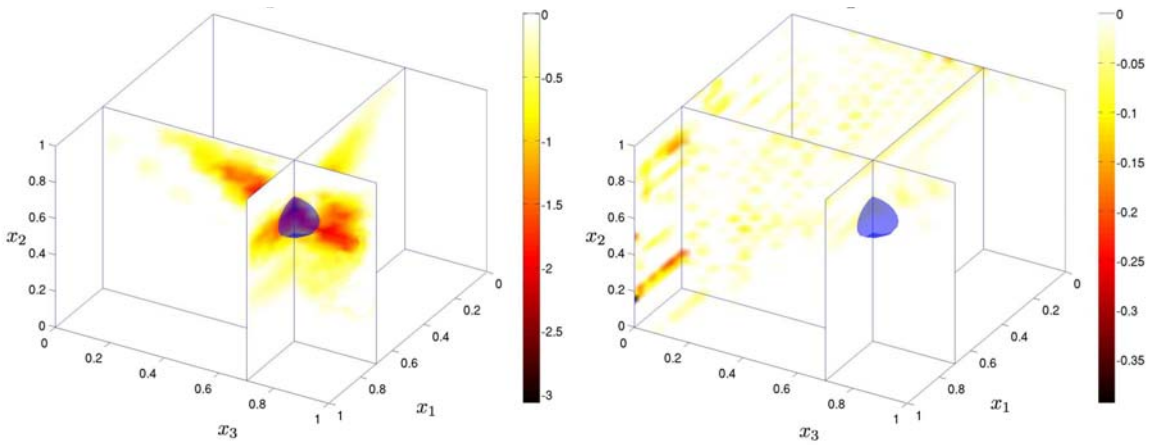

(a) $S^{\text{obs}} = \{\xi_2 = 1\}$ (b) $S^{\text{obs}} = \{\xi_3 = 0\}$

Figure 18: *Influence of limited aperture: distribution of* $\mathbb{T}_\alpha$ *for two choices of* S^{obs}.

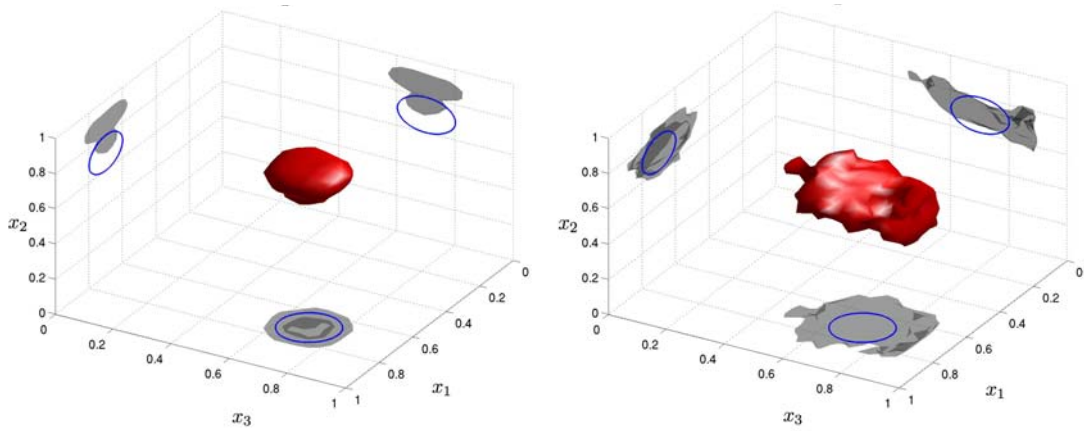

(a) $S^{\text{obs}} = \{\xi_2 = 1\}$ (b) $S^{\text{obs}} = \{\xi_3 = 1\}$

Figure 19: *Influence of limited aperture: $B_{eq}(\alpha)$ for two choices of partial observation surface S^{obs}.*

solid, and the horiozontal location of the sought cavity is correctly found while its vertical estimated position is offset compared to the correct one. For data collected on the lateral face $\xi_3 = 0$ (Fig. 18(b)), the TS field does not resolve correctly the unknown cavity. Moreover, plots of $B_{\text{eq}}(\alpha)$ corresponding to observations surfaces $S^{\text{obs}} = \{\xi_2 = 1\}$ and $S^{\text{obs}} = \{\xi_3 = 1\}$ (chosen closest to B^{true} to yield sufficient usable data) indicate satisfactory reconstruction of B^{true} (Fig. 19). For the two cases shown, B_{true} is better estimated along the direction orthogonal to S^{obs}, with the best identification obtained in Fig. 19(a) corresponding to S^{obs} orthogonal to the propagation direction of the incident wave.

6.5 Influence of data noise

In this section the influence of data noise is studied by considering noisy simulated data of the form

$$\boldsymbol{u}_h^{\text{obs}}(\cdot, t_j) = \boldsymbol{u}_h^{\text{true}}(\cdot, t_j) + \sigma \chi \boldsymbol{u}_j^{\text{max}}, \quad \boldsymbol{u}_j^{\text{max}} = \Big\{ \max_{1 \le i \le n^{\text{obs}}} \Big(\big[\boldsymbol{u}_h^{\text{true}}(\boldsymbol{\xi}_i, t_j) - \boldsymbol{u}_h(\boldsymbol{\xi}_i, t_j) \big] \cdot \boldsymbol{e}_k \Big) \Big\} \boldsymbol{e}_k \quad (42)$$

where χ is a Gaussian random variable with zero mean and unit standard deviation. Figure 20 depicts the behavior of the imaging method for increasing noise level σ. Remarkably, the cavity location is correctly estimated even for high noise levels (Figs. 20(c) and 20(d)). TS-based identification thus still yields usable results if applied to noisy data, as anticipated in Sec. 4.1 based on the mathematical structure of the TS formula, even though no regularization is used in the cost functional. This feature is very promising for applications. Note that the reference $\boldsymbol{u}_h^{\text{true}}$ used in (42) is itself "noisy", being a FEM-based approximation of $\boldsymbol{u}^{\text{true}}$. The discretization error level thus superimposed to the simulated data noise is expected not to exceed a few percent in the examples presented here (and thus to be much lower than the noise levels of Figs. 20(c) and 20(d)). For instance, synthetic data evaluations for the 2D elastodynamic examples presented a $2.1\,10^{-2}$ relative discrepancy (in L^2-norm) when performed on meshes featuring 2420 and 5453 nodes.

6.6 Identification of non-cavity defects

To conclude this series of numerical experiments, the identification of a crack and an inclusion is now considered, whose geometrical or material characteristics do not conform to those assumed in deriving the topological sensitivity.

Crack identification. The identification of a penny-shaped crack (radius $R = 0.1$, unit normal $\boldsymbol{n} = -\sin\theta \boldsymbol{e}_1 + \cos\theta \boldsymbol{e}_2$) leads to results that are satisfactory in terms of crack location and size, as shown in Fig. 21 for two choices $\theta = 0$ and $\theta = \pi/4$ of the crack inclination, while lacking sensitivity to the crack inclination. A recently-proposed specific formulation for crack problems (Bellis and Bonnet, 2009) features a polarization tensor that depends explicitly on an assumed crack orientation, thus offering (not yet investigated) possibilities for finding the crack orientation on that basis.

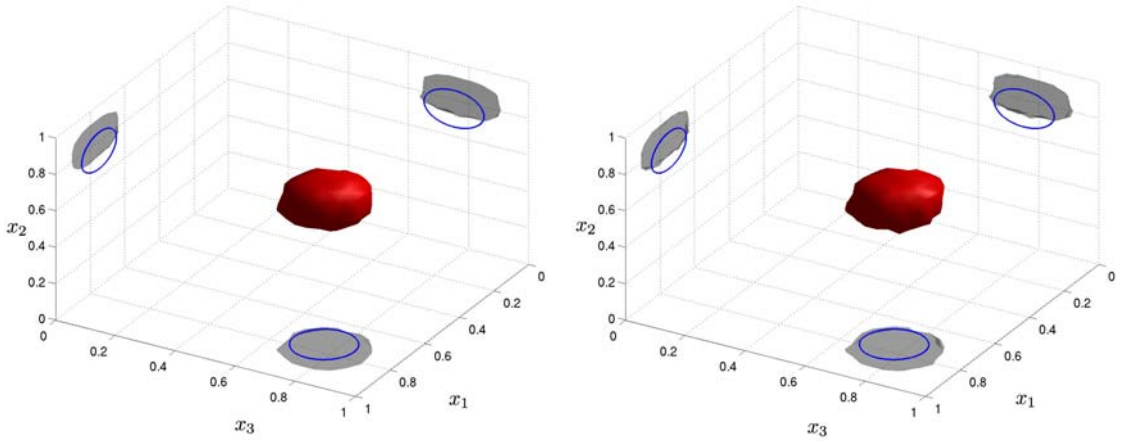

(a) $\sigma = 0.1$, $\boldsymbol{x}^{\text{true}} = (0.75,\ 0.75,\ 0.75)$, $\alpha = 0.75$ (b) $\sigma = 0.2$, $\boldsymbol{x}^{\text{true}} = (0.75,\ 0.75,\ 0.75)$, $\alpha = 0.75$

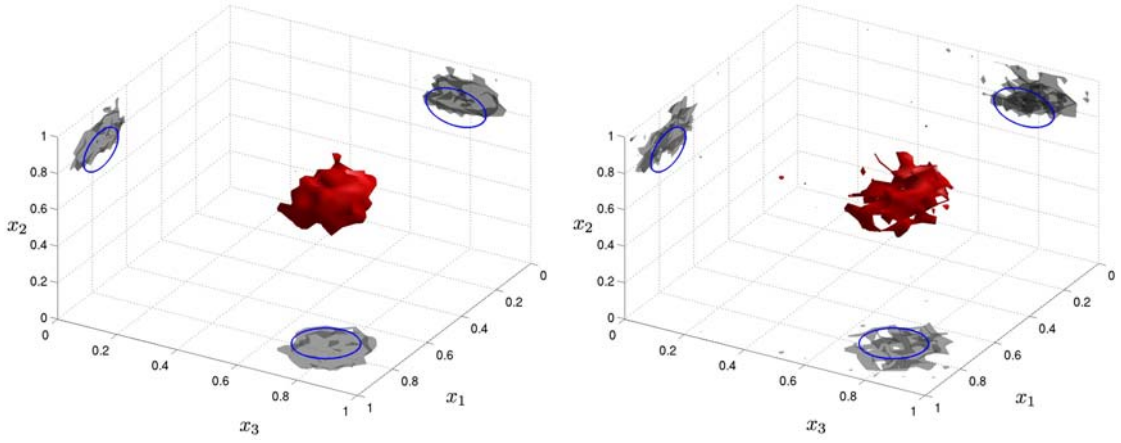

(c) $\sigma = 0.5$, $\boldsymbol{x}^{\text{true}} = (0.75,\ 0.75,\ 0.75)$, $\alpha = 0.75$ (d) $\sigma = 1$, $\boldsymbol{x}^{\text{true}} = (0.75,\ 0.75,\ 0.75)$, $\alpha = 0.6$

Figure 20: *Influence of data noise on* $\mathbb{T}$*:* $B_{eq}(\alpha)$ *for various levels of noise.*

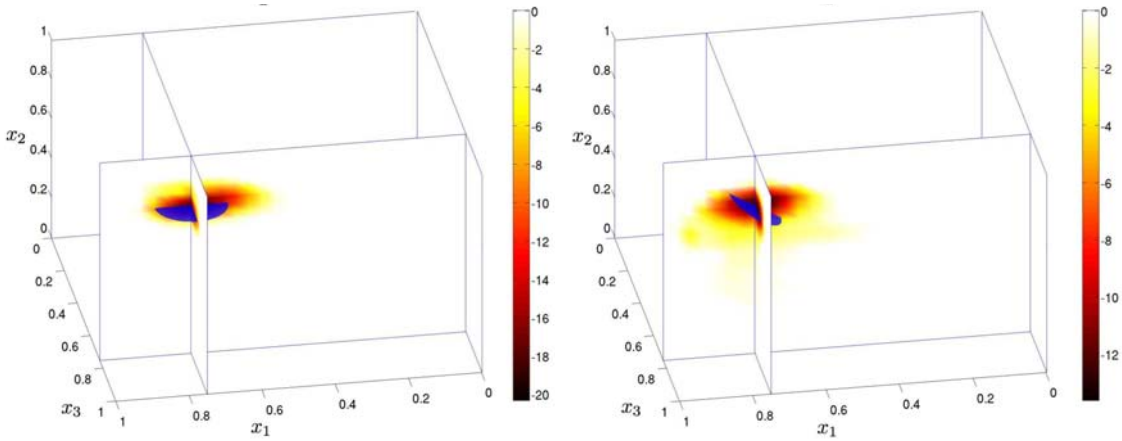

(a) $\theta = 0$ (horizontal), $\alpha = 0$, $\boldsymbol{x}^{\text{true}} = (0.75,\ 0.75,\ 0.75)$ (b) $\theta = \pi/4$ (inclined), $\alpha = 0$, $\boldsymbol{x}^{\text{true}} = (0.75,\ 0.75,\ 0.75)$

Figure 21: *Penny-shaped crack identification: thresholded TS field* $\mathbb{T}_{\alpha}$.

Inclusion identification. The identification of a penetrable spherical inclusion characterized by the radius $R = 0.1$ and material parameters $\mu^\star,\ \nu^\star = \nu,\ \rho^\star = \rho$ is now considered. The TS defined for cavities is found to identify satisfactorily *soft* spherical inclusions (such that $\mu^\star \leqslant \mu$), see Fig. 22. However, employing this method for *stiff* inclusions (such that $\mu^\star > \mu$) leads to an contrast inversion in the TS field, the defect location now corresponding to a *maximum* of $\mathbb{T}(\cdot, T)$. Moreover, the TS defined for spherical elastic inclusions with assumed material parameters $\mu^\star, \nu^\star, \rho^\star$, given by

$$\mathbb{T}^\star(\boldsymbol{z}, T) = \{\boldsymbol{\sigma}[\hat{\boldsymbol{u}}] \star (\boldsymbol{\mathcal{A}}^\star : \boldsymbol{\sigma}[\boldsymbol{u}]) + (\rho - \rho^\star)\ddot{\hat{\boldsymbol{u}}} \star \ddot{\boldsymbol{u}}\}(\boldsymbol{z}, T) \tag{43}$$

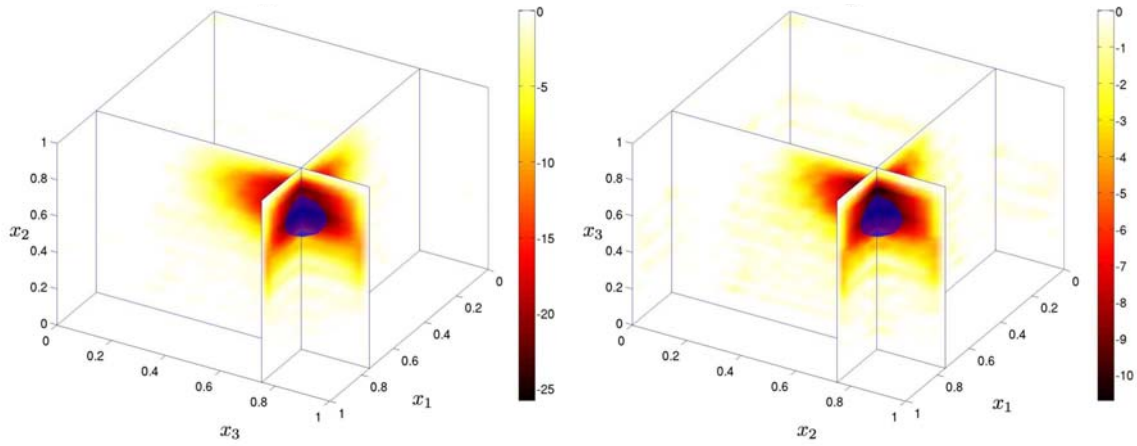

(a) $\mu^\star = 0.1\mu$, $\alpha = 0$, $\boldsymbol{x}^{\text{true}} = (0.75,\ 0.75,\ 0.75)$ (b) $\mu^\star = 0.5\mu$, $\alpha = 0$, $\boldsymbol{x}^{\text{true}} = (0.75,\ 0.75,\ 0.75)$

Figure 22: *Identification of a soft spherical inclusion using cavity-related thresholded TS field* $\mathbb{T}_\alpha$.

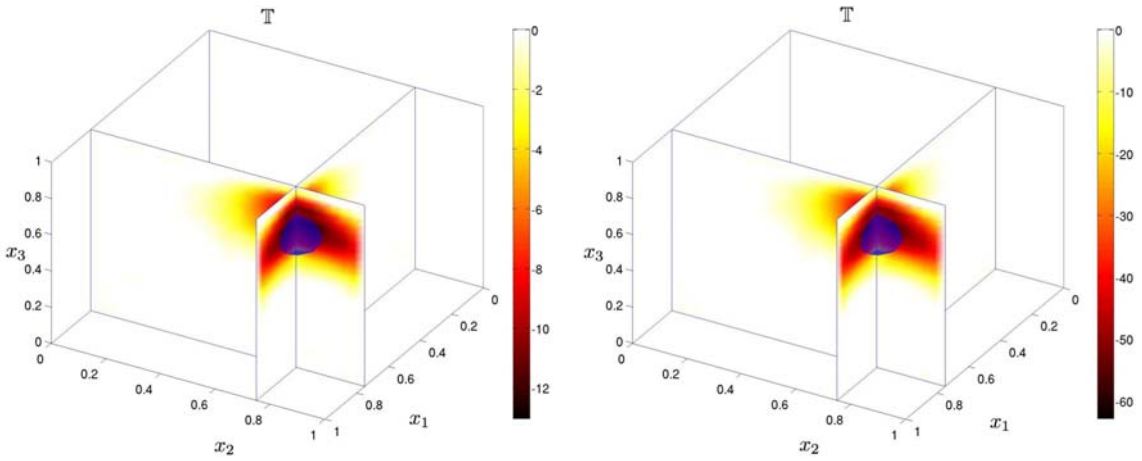

(a) $\mu^\star = 5\mu$, $\alpha = 0$, $\boldsymbol{x}^{\text{true}} = (0.75,\ 0.75,\ 0.75)$ (b) $\mu^\star = 10\mu$, $\alpha = 0$, $\boldsymbol{x}^{\text{true}} = (0.75,\ 0.75,\ 0.75)$

Figure 23: *Identification of a stiff spherical inclusion using inclusion-related thresholded TS field* $\mathbb{T}^\star_\alpha$.

with the polarization tensor $\boldsymbol{\mathcal{A}}^\star$ given by (B.2) and established in Chikichev and Guzina (2008), has also been implemented within the present FEM approach. Then, the TS field $\mathbb{T}^\star$ computed for the correct values of $\mu^\star, \nu^\star, \rho^\star$ is seen in Fig. 23 to allow a correct identification of a stiff inclusion.

7 Conclusion

In this study, the concept of topological sensitivity (TS) is developed for elastic and acoustic-wave imaging of media of arbitrary geometry using data in the time domain. On seeking the limiting form of the boundary integral equation governing the scattered field caused by a cavity with vanishing size ε, the TS field is found to be expressed in terms of the time convolution of the free field and an adjoint field. The ε^{D} asymptotic behavior of the cost function revealed by the analysis, identical to that established earlier for identification in static of frequency-domain settings, requires a degree of smoothness of the free field with respect to the time variable. The main analysis is devoted to 3-D configurations, but 2-D time-domain formulations are addressed as well.

While its derivation and formulation results from a mathematically rigorous asymptotic analysis, subsequent applications of the TS concept to the identification of finite-sized defects remains heuristic. Here, a comprehensive set of numerical examples is presented so as to substantiate the usefulness of the TS in applications and assess its performances. In contrast with the relatively involved analysis required to arrive at the correct formulation of the TS field, subsequent numerical implementations

are quite simple. To emphasize the ease of application of the TS concept, all examples presented in this article rely on straightforward FEM formulations of the free and adjoint field, rather than more-specialized integral-equation techniques previously used by the same group of authors. Several important features of the method are discussed through these examples, including its ability to identify multiple defects or to withstand significant data noise, and the effect of restrictions on the data through insufficient experiment duration or partial aperture. It is important to note that most examples consider identification based on a *single* (simulated) time-domain experiment.

From this study, it can be concluded that computing and exploiting the TS field constitutes a powerful and efficient tool for defect identification, as it is very simple to implement, computationally much faster than minimization-based inversion methods, and allows multiple defect identification without prior information. The present "one-shot" TS-based identification is qualitative rather than quantitative in nature. In addition to the stand-alone one-shot TS-based procedure emphasized in this article (of a qualitative rather than quantitative nature, and hence useful if speed or ease of implementation is more important than accurate defect sizing), the TS may also be implemented using an iterative matter removal strategy of the kind used in topology optimization (Allaire et al., 2005; Garreau et al., 2001), or be used in computing good initial guesses for subsequent refined inversion (perhaps based on exploiting $B_{\text{eq}}(\alpha)$ and $R_{\text{eq}}(\alpha)$ defined by (37), (38)). Quantitative defect identification may also be achieved on the basis of time-domain versions (to be developed) of higher-order topological expansions along the lines of Bonnet (2008, 2009).

References

Achenbach, J. D., 2003. *Reciprocity in elastodynamics*. Cambridge University Press.

Allaire, G., de Gournay, F., Jouve, F., Toader, A.-M., 2005. Structural optimization using topological and shape sensitivity via a level-set method. *Control and Cybernetics*, **34**:59–80.

Ammari, H., Guadarrama Bustos, L., Garapon, P., Kang, H., 2009. Transient anomaly imaging by the acoustic radiation force. Preprint, http://www.cmap.polytechnique.fr/∼ammari/papers/RFI_supp-1.pdf.

Ammari, H., Kang, H., 2004. *Reconstruction of small inhomogeneities from boundary measurements*. Lecture Notes in Mathematics 1846. Springer-Verlag.

Ammari, H., Kang, H., 2006. Reconstruction of elastic inclusions of small volume via dynamic measurements. *Appl. Math. Opt.*, **54**:223–235.

Ammari, H., Kang, H., 2007. *Polarization and Moment Tensors With Applications to Inverse Problems and Effective Medium Theory*. Applied Mathematical Sciences , Vol. 162. Springer-Verlag.

Arens, T., 2001. Linear sampling methods for 2D inverse elastic wave scattering. *Inverse Problems*, **17**:1445–1464.

Bellis, C., Bonnet, M., 2009. Crack identification by 3D time-domain elastic or acoustic topological sensitivity. *Comptes Rendus Mécanique*, **337**:124–130.

Bonnet, M., 1995. BIE and material differentiation applied to the formulation of obstacle inverse problems. *Engng. Anal. with Bound. Elem.*, **15**:121–136.

Bonnet, M., 2006. Topological sensitivity for 3D elastodynamic and acoustic inverse scattering in the time domain. *Comp. Meth. Appl. Mech. Engng.*, **195**:5239–5254.

Bonnet, M., 2008. Inverse acoustic scattering by small-obstacle expansion of misfit function. *Inverse Problems*, **24**:035022.

Bonnet, M., 2009. Higher-order topological sensitivity for 2-D potential problems. Application to fast identification of inclusions. *Int. J. Solids Struct.*, **46**:2275–2292.

Bonnet, M., Guzina, B. B., 2004. Sounding of finite solid bodies by way of topological derivative. *Int. J. Num. Meth. in Eng.*, **61**:2344–2373.

Bonnet, M., Guzina, B. B., 2009. Elastic-wave identification of penetrable obstacles using shape-material sensitivity framework. *J. Comp. Phys.*, **228**:294–311.

Cassereau, D., Wu, F., Fink, M., 1990. Limits of self-focusing using closed time-reversal cavities and mirrors - Theory and experiment. In *IEEE Ultrasonics Symposium, vol. 3*, 1613–1618.

Chikichev, I., Guzina, B. B., 2008. Generalized topological derivative for the Navier equation and inverse scattering in the time domain. *Comp. Meth. Appl. Mech. Engng.*, **197**:4467–4484.

Colton, D., Kirsch, A., 1996. A simple method for solving inverse scattering problems in the resonance region. *Inverse Problems*, **12**:383–393.

Colton, D., Kress, R., 1998. *Inverse acoustic and electromagnetic scattering theory*. Springer-Verlag.

Dominguez, N., Gibiat, V., Esquerré, Y., 2005. Time domain topological gradient and time reversal analogy: an inverse method for ultrasonic target detection. *Wave Motion*, **42**:31–52.

Eringen, A. C., Suhubi, E. S., 1975. *Elastodynamics (vol II - linear theory)*. Academic Press.

Eschenauer, H. A., Kobelev, V. V., Schumacher, A., 1994. Bubble method for topology and shape optimization of structures. *Structural Optimization*, **8**:42–51.

Feijóo, G. R., 2004. A new method in inverse scattering based on the topological derivative. *Inverse Problems*, **20**:1819–1840.

Gallego, R., Rus, G., 2004. Identification of cracks and cavities using the topological sensitivity boundary integral equation. *Comp. Mech.*, **33**:154–163.

Garreau, S., Guillaume, P., Masmoudi, M., 2001. The topological asymptotic for PDE systems: the elasticity case. *SIAM J. Contr. Opt.*, **39**:1756–1778.

Guzina, B. B., Bonnet, M., 2004. Topological derivative for the inverse scattering of elastic waves. *Quart. J. Mech. Appl. Math.*, **57**:161–179.

Guzina, B. B., Bonnet, M., 2006. Small-inclusion asymptotic of misfit functionals for inverse problems in acoustics. *Inverse Problems*, **22**:1761–1785.

Hughes, T. J. R., 1987. *The finite element method – linear static and dynamic finite element analysis*. Prentice Hall, Englewood Cliffs, New Jersey, USA.

Jackowska-Strumillo, L., Sokolowski, J., Zochowski, A., 2002. Topological optimization and inverse problems. *Computer Assisted Mechanics and Engineering Sciences*, **10**(2):163–176.

Malcolm, A., Guzina, B., 2008. On the topological sensitivity of transient acoustic fields. *Wave Motion*, **45**:821–834.

Masmoudi, M., Pommier, J., Samet, B., 2005. The topological asymptotic expansion for the Maxwell equations and some applications. *Inverse Problems*, **21**:547–564.

Nintcheu Fata, S., Guzina, B. B., 2004. A linear sampling method for near-field inverse problems in elastodynamics. *Inverse Problems*, **20**:713–736.

Nintcheu Fata, S., Guzina, B. B., 2007. Elastic scatterer reconstruction via the adjoint sampling method. *SIAM J. Appl. Math.*, **67**:1330–1352.

Potthast, R., 2006. A survey on sampling and probe methods for inverse problems. *Inverse Problems*, **22**:R1–R47.

Schumacher, A., 1995. *Topologieoptimierung von Bauteilstrukturen unter Verwendung von Lochpositionierungskriterien*. Ph.D. thesis, Univ. of Siegen, Germany.

Sokolowski, J., Zochowski, A., 1999. On the topological derivative in shape optimization. *SIAM J. Control Optim.*, **37**:1251–1272.

Appendix A Asymptotic behaviour of elastodynamic integral operators

Appendix A.1 Elastodynamic governing BIE

The integral representation formula for the scattered field $\boldsymbol{v}^\varepsilon$ reads (Eringen and Suhubi, 1975)

$$\boldsymbol{v}^\varepsilon(\boldsymbol{x},t) = -\int_{\Gamma_\varepsilon(z)} \left\{ \boldsymbol{T}(\boldsymbol{x},t,\boldsymbol{\xi};\boldsymbol{n}) \star \boldsymbol{v}^\varepsilon(\boldsymbol{\xi},t) + \boldsymbol{U}(\boldsymbol{x},t,\boldsymbol{\xi}) \star \boldsymbol{t}[\boldsymbol{u}](\boldsymbol{\xi},t) \right\} \mathrm{d}S_\xi \tag{A.1}$$

In the present situation, where the free field featured in the right-hand side of (A.1) is also defined *inside* the cavity region $B_\varepsilon(\boldsymbol{z})$, one has

$$-\int_{\Gamma_\varepsilon(z)} \boldsymbol{U}(\boldsymbol{x},t,\boldsymbol{\xi}) \star \boldsymbol{t}[\boldsymbol{u}](\boldsymbol{\xi},t)\, \mathrm{d}S_\xi = \int_{B_\varepsilon(z)} \left[\rho \boldsymbol{U}(\boldsymbol{x},t,\boldsymbol{\xi}) \star \ddot{\boldsymbol{u}}(\boldsymbol{\xi},t) + \boldsymbol{E}(\boldsymbol{x},t,\boldsymbol{\xi}) \star \boldsymbol{\sigma}[\boldsymbol{u}](\boldsymbol{\xi},t)\right] \mathrm{d}V_\xi$$

by virtue of the divergence formula (note that $-\boldsymbol{n}$ in (A.1) is the *outward* unit normal to $B_\varepsilon(\boldsymbol{z})$) and the field equation (9a) verified by $\boldsymbol{u}$. Integral equation (13) then follows by invoking the following property of time convolution (14), easily established using integration by parts and conditions (15):

$$[\boldsymbol{a} \star \ddot{\boldsymbol{b}}](\boldsymbol{\xi},t) = [\dot{\boldsymbol{a}} \star \dot{\boldsymbol{b}}](\boldsymbol{\xi},t) = [\ddot{\boldsymbol{a}} \star \boldsymbol{b}](\boldsymbol{\xi},t)$$

Appendix A.2 Elastodynamic fundamental solutions and proof of Lemmas 1 to 3

The time convolutions featured in integral equation (13) can be expressed as

$$\boldsymbol{U}(\boldsymbol{x},t,\boldsymbol{\xi}) \star \boldsymbol{t}(\boldsymbol{\xi},t) = \boldsymbol{U}[\boldsymbol{x},t,\boldsymbol{\xi}|\boldsymbol{e}_i \cdot \boldsymbol{t}(\boldsymbol{\xi},\cdot)] \cdot \boldsymbol{e}_i \tag{A.2a}$$

$$\boldsymbol{T}(\boldsymbol{x},t,\boldsymbol{\xi};\boldsymbol{n}) \star \boldsymbol{v}^\varepsilon(\boldsymbol{\xi},t) = \boldsymbol{T}[\boldsymbol{x},t,\boldsymbol{\xi};\boldsymbol{n}|\boldsymbol{e}_i \cdot \boldsymbol{v}^\varepsilon(\boldsymbol{\xi},\cdot)] \cdot \boldsymbol{e}_i \tag{A.2b}$$

where $\boldsymbol{U}[\boldsymbol{x},t,\boldsymbol{\xi}|f]$ and $\boldsymbol{T}[\boldsymbol{x},t,\boldsymbol{\xi};\boldsymbol{n}|f]$ are the time-modulated elastodynamic Green's tensors, defined such that $\boldsymbol{e}_k \cdot \boldsymbol{U}$ and $\boldsymbol{e}_k \cdot \boldsymbol{T}$ are the displacement and traction vectors at $\boldsymbol{\xi} \in \Omega$ resulting from a point force acting at $\boldsymbol{x}$ in the k-direction with prescribed time-varying magnitude $f(t)$. The latter solve the boundary-initial value problem

$$\mathcal{L}_\xi \boldsymbol{U}[\boldsymbol{x},t,\boldsymbol{\xi}|f] + \delta(\boldsymbol{\xi}-\boldsymbol{x}) f(t) \boldsymbol{I} = \boldsymbol{0} \qquad (\boldsymbol{\xi} \in \Omega, t \geqslant 0) \tag{A.3a}$$

$$\boldsymbol{T}[\boldsymbol{x},t,\boldsymbol{\xi};\boldsymbol{n}|f] = \boldsymbol{0} \qquad (\boldsymbol{\xi} \in S_\mathrm{N}, t \geqslant 0) \tag{A.3b}$$

$$\boldsymbol{U}[\boldsymbol{x},t,\boldsymbol{\xi}|f] = \boldsymbol{0} \qquad (\boldsymbol{\xi} \in S_\mathrm{D}, t \geqslant 0) \tag{A.3c}$$

$$\boldsymbol{U}[\boldsymbol{x},0,\boldsymbol{\xi}|f] = \dot{\boldsymbol{U}}[\boldsymbol{x},0,\boldsymbol{\xi}|f] = \boldsymbol{0} \qquad (\boldsymbol{\xi} \in \Omega) \tag{A.3d}$$

Similarly, let $\boldsymbol{U}_\infty[\boldsymbol{x},t,\boldsymbol{\xi}|f]$ and $\boldsymbol{T}_\infty[\boldsymbol{x},t,\boldsymbol{\xi};\boldsymbol{n}|f]$ denote the time-modulated infinite-space fundamental solution, which satisfy equations (A.3a), (A.3d) with $\Omega = \mathbb{R}^3$ and radiation conditions instead of boundary conditions (A.3b), (A.3c), and is given by (Eringen and Suhubi, 1975)

$$\boldsymbol{U}_\infty[\boldsymbol{x},t,\boldsymbol{\xi}|f] = \frac{1}{4\pi\mu r}\Big[A[\boldsymbol{x},t,\boldsymbol{\xi}|f]\, \boldsymbol{I} + B[\boldsymbol{x},t,\boldsymbol{\xi}|f]\, (\hat{\boldsymbol{r}} \otimes \hat{\boldsymbol{r}})\Big] \tag{A.4a}$$

$$\boldsymbol{E}[\boldsymbol{x},t,\boldsymbol{\xi}|f] = \frac{1}{8\pi\mu r^2}\Big[B[\boldsymbol{x},t,\boldsymbol{\xi}|f](\hat{\boldsymbol{r}} \otimes \boldsymbol{I}) + D[\boldsymbol{x},t,\boldsymbol{\xi}|f](\boldsymbol{\mathcal{I}}^{\mathrm{sym}} \cdot \hat{\boldsymbol{r}}) + 2E[\boldsymbol{x},t,\boldsymbol{\xi}|f](\hat{\boldsymbol{r}} \otimes \hat{\boldsymbol{r}} \otimes \hat{\boldsymbol{r}})\Big] \tag{A.4b}$$

$$\begin{aligned}\boldsymbol{T}_\infty[\boldsymbol{x},t,\boldsymbol{\xi};\boldsymbol{n}|f] = \frac{1}{4\pi r^2}\Big[&C[\boldsymbol{x},t,\boldsymbol{\xi}|f]\, (\hat{\boldsymbol{r}} \otimes \boldsymbol{n}) + D[\boldsymbol{x},t,\boldsymbol{\xi}|f]\, \big(\hat{\boldsymbol{r}} \otimes \boldsymbol{n} + (\hat{\boldsymbol{r}} \cdot \boldsymbol{n})\boldsymbol{I}\big) \\ &+ 2E[\boldsymbol{x},t,\boldsymbol{\xi}|f]\, (\boldsymbol{n} \cdot \hat{\boldsymbol{r}})\hat{\boldsymbol{r}} \otimes \hat{\boldsymbol{r}}\Big]\end{aligned} \tag{A.4c}$$

where $\boldsymbol{r} = (\boldsymbol{\xi} - \boldsymbol{x})$, $r = \|\boldsymbol{r}\|$, $\hat{\boldsymbol{r}} = \boldsymbol{r}/r$, κ is the ratio of bulk wave velocities as defined by

$$\kappa^2 = \frac{c_T^2}{c_L^2} = \frac{1-2\nu}{2(1-\nu)} = \frac{\mu}{\lambda + 2\mu} \tag{A.5}$$

and with $A = A[\boldsymbol{x},t,\boldsymbol{\xi}|f],\ldots$ defined by

$$\begin{aligned}
A[\boldsymbol{x},t,\boldsymbol{\xi}|f] &= f\Big(t-\frac{r}{c_T}\Big) + \int_1^\kappa \eta f\Big(t-\frac{\eta r}{c_T}\Big)\,\mathrm{d}\eta \\
B[\boldsymbol{x},t,\boldsymbol{\xi}|f] &= -3A[\boldsymbol{x},t,\boldsymbol{\xi}|f] + 2f\Big(t-\frac{r}{c_T}\Big) + \kappa^2 f\Big(t-\frac{r}{c_L}\Big) \\
C[\boldsymbol{x},t,\boldsymbol{\xi}|f] &= 2B[\boldsymbol{x},t,\boldsymbol{\xi}|f] - (1-2\kappa^2)\Big\{f\Big(t-\frac{r}{c_L}\Big) + \frac{r}{c_L}\dot f\Big(t-\frac{r}{c_L}\Big)\Big\} \\
D[\boldsymbol{x},t,\boldsymbol{\xi}|f] &= 2B[\boldsymbol{x},t,\boldsymbol{\xi}|f] - f\Big(t-\frac{r}{c_T}\Big) - \frac{r}{c_T}\dot f\Big(t-\frac{r}{c_T}\Big) \\
E[\boldsymbol{x},t,\boldsymbol{\xi}|f] &= -3B[\boldsymbol{x},t,\boldsymbol{\xi}|f] - D[\boldsymbol{x},t,\boldsymbol{\xi}|f] - \kappa^2\Big\{f\Big(t-\frac{r}{c_L}\Big) + \frac{r}{c_L}\dot f\Big(t-\frac{r}{c_L}\Big)\Big\}.
\end{aligned} \tag{A.6}$$

Define now the time-modulated complementary elastodynamic Green's tensor $\boldsymbol{U}_{\mathrm{C}}$ by

$$\boldsymbol{U}[\boldsymbol{x},t,\boldsymbol{\xi}|f] = \boldsymbol{U}_\infty[\boldsymbol{x},t,\boldsymbol{\xi}|f] + \boldsymbol{U}_{\mathrm{C}}[\boldsymbol{x},t,\boldsymbol{\xi}|f] \tag{A.7}$$

By virtue of superposition arguments, $\boldsymbol{U}_{\mathrm{C}}$ is governed by the boundary-initial value problem

$$\begin{aligned}
\mathcal{L}_\xi \boldsymbol{U}_{\mathrm{C}}[\boldsymbol{x},t,\boldsymbol{\xi}|f] &= \boldsymbol{0} && (\boldsymbol{\xi}\in\Omega, t\geqslant 0) \\
\boldsymbol{T}_{\mathrm{C}}[\boldsymbol{x},t,\boldsymbol{\xi};\boldsymbol{n}|f] &= -\boldsymbol{T}_\infty[\boldsymbol{x},t,\boldsymbol{\xi};\boldsymbol{n}|f] && (\boldsymbol{\xi}\in S_{\mathrm{N}}, t\geqslant 0) \\
\boldsymbol{U}_{\mathrm{C}}[\boldsymbol{x},t,\boldsymbol{\xi}|f] &= -\boldsymbol{U}_\infty[\boldsymbol{x},t,\boldsymbol{\xi}|f] && (\boldsymbol{\xi}\in S_{\mathrm{D}}, t\geqslant 0) \\
\boldsymbol{U}_{\mathrm{C}}[\boldsymbol{x},0,\boldsymbol{\xi}|f] = \dot{\boldsymbol{U}}_{\mathrm{C}}[\boldsymbol{x},0,\boldsymbol{\xi}|f] &= \boldsymbol{0} && (\boldsymbol{\xi}\in\Omega)
\end{aligned} \tag{A.8}$$

One can then show (using e.g. an integral representation formula) that $\boldsymbol{U}_{\mathrm{C}}[\boldsymbol{x},t,\boldsymbol{\xi}|f]$ is bounded in the limit $\boldsymbol{\xi}\to\boldsymbol{x}$, i.e. that the singular behavior of $\boldsymbol{U}[\boldsymbol{x},t,\boldsymbol{\xi}|f]$ at $\boldsymbol{\xi}=\boldsymbol{x}$ is identical to that of its full-space counterpart $\boldsymbol{U}_\infty[\boldsymbol{x},t,\boldsymbol{\xi}|f]$. Hence, one has

$$\boldsymbol{U}_{\mathrm{C}}[\boldsymbol{z}+\varepsilon\bar{\boldsymbol{x}},t,\boldsymbol{z}+\varepsilon\bar{\boldsymbol{\xi}}|f] = O(1) \qquad (\varepsilon\to 0) \tag{A.9}$$

Proof of Lemma 1. With decomposition (A.7) of $\boldsymbol{U}[\boldsymbol{x},t,\boldsymbol{\xi}|f]$ in mind, consider first the evaluation of the leading contribution to

$$\int_{\Gamma_\varepsilon(z)} \boldsymbol{U}_\infty(\boldsymbol{x},t,\boldsymbol{\xi}) \star \boldsymbol{t}(\boldsymbol{\xi},t)\,\mathrm{d}S_\xi \tag{A.10}$$

as $\varepsilon\to 0$, where $\boldsymbol{U}_\infty(\boldsymbol{x},t,\boldsymbol{\xi})\star\boldsymbol{t}(\boldsymbol{\xi},t)$ is, by virtue of (A.2a), given by (A.4a) with $f(t)=\boldsymbol{e}_i\cdot t(\boldsymbol{\xi},t)$. Setting $f(\tau)=f(t)+(f(\tau)-f(t))=f(t)+\Delta f(\tau)=$ in (A.6), one obtains

$$A[\boldsymbol{x},t,\boldsymbol{\xi}|f] = \frac{1+\kappa^2}{2}f(t) + A[\boldsymbol{x},t,\boldsymbol{\xi}|\Delta f], \quad B[\boldsymbol{x},t,\boldsymbol{\xi}|f] = \frac{1-\kappa^2}{2}f(t) + B[\boldsymbol{x},t,\boldsymbol{\xi}|\Delta f]. \tag{A.11}$$

The cofactors of $f(t)$ in (A.11) correspond to a *constant* point force of unit magnitude, and hence yield, through (A.4a), the *elastostatic* full-space Green's tensor (i.e. Kelvin's solution) $\boldsymbol{U}_\infty(\bar{\boldsymbol{x}},\bar{\boldsymbol{\xi}})$:

$$\boldsymbol{U}_\infty(\bar{\boldsymbol{x}},\bar{\boldsymbol{\xi}}) = \frac{1}{8\pi\mu\bar r}\big[(1+\kappa^2)\boldsymbol{I} + (1-\kappa^2)\hat{\bar{\boldsymbol{r}}}\otimes\hat{\bar{\boldsymbol{r}}}\big] \tag{A.12}$$

Moreover, the Lipschitz-continuity assumption made on $t\mapsto\boldsymbol{\sigma}[\boldsymbol{u}](\boldsymbol{\xi},t)$ implies that

$$|f(t)-f(\tau)|\leqslant K|t-\tau|, \quad |\dot f(\tau)|\leqslant K \qquad 0\leqslant\tau\leqslant t$$

(with K the Lipschitz continuity modulus of f) and hence that

$$A[\boldsymbol{x},t,\boldsymbol{\xi}|\Delta f]\leqslant KC_{\mathrm{A}}r/c_{\mathrm{T}}, \qquad B[\boldsymbol{x},t,\boldsymbol{\xi}|\Delta f]\leqslant KC_{\mathrm{B}}r/c_{\mathrm{T}} \tag{A.13}$$

with appropriate constants $C_{\mathrm{A}}, C_{\mathrm{B}}$. Combining (A.4a), (A.11) and (A.13), one thus obtains

$$\boldsymbol{U}_\infty(\boldsymbol{x},t,\boldsymbol{\xi})\star\boldsymbol{t}(\boldsymbol{\xi},t) = \boldsymbol{U}_\infty(\boldsymbol{x},\boldsymbol{\xi})\cdot\boldsymbol{t}(\boldsymbol{\xi},t) + \boldsymbol{U}_\infty(\boldsymbol{x},t,\boldsymbol{\xi})\star\Delta\boldsymbol{t}(\boldsymbol{\xi},t),$$

$$\big\| \boldsymbol{U}_\infty(\boldsymbol{x},t,\boldsymbol{\xi}) \star \Delta\boldsymbol{t}(\boldsymbol{\xi},t) \big\| \leqslant C_{\mathrm{U}} K, \tag{A.14}$$

where C_{U} is a constant. Hence, upon introducing scaling (16), (17) into (A.10), noting that $\boldsymbol{U}_\infty(\boldsymbol{\xi},\boldsymbol{x})$ is homogeneous of degree -1 in $\bar{\boldsymbol{\xi}}-\bar{\boldsymbol{x}}$, making use of the expansion $\boldsymbol{\sigma}[\boldsymbol{u}](\boldsymbol{\xi},t) = \boldsymbol{\sigma}[\boldsymbol{u}](\boldsymbol{z},t)+o(1)$, and invoking (A.14), one obtains

$$\int_{\Gamma_\varepsilon(z)} \boldsymbol{U}_\infty(\boldsymbol{x},t,\boldsymbol{\xi}) \star \boldsymbol{t}(\boldsymbol{\xi},t)\ \mathrm{d}S_\xi = \varepsilon\bigg\{\int_{\mathcal{S}} \boldsymbol{U}_\infty(\bar{\boldsymbol{x}},\bar{\boldsymbol{\xi}}) \otimes \boldsymbol{n}(\bar{\boldsymbol{\xi}})\ \mathrm{d}\bar{S}_{\bar{\xi}}\bigg\} : \boldsymbol{\sigma}[\boldsymbol{u}](\boldsymbol{z},t) + o(\varepsilon) \tag{A.15}$$

Finally, Lemma 1 follows from (A.7), (A.15) together with the following estimate stemming from (A.9):

$$\int_{\Gamma_\varepsilon(z)} \boldsymbol{U}_{\mathrm{C}}(\boldsymbol{x},t,\boldsymbol{\xi}) \star \boldsymbol{t}(\boldsymbol{\xi},t)\ \mathrm{d}S_\xi = O(\varepsilon^2). \tag{A.16}$$

Remark 6. *The presence of $r\dot{f}(t-r/c_{L,T})$ in expressions (A.6) of C, D, E implies that the fundamental strains $\boldsymbol{E}[\boldsymbol{x},t,\boldsymbol{\xi}|f]$ and stresses behave as $O(r^{-1})$ in the time-modulated case ($\dot{f}\neq 0$) but as as $O(r^{-2})$ in the static case ($\dot{f}=0$).*

Proof of Lemma 2. The proof again exploits decomposition (A.7). First, upon introducing scaled coordinates (16) into expression (A.4c) of $\boldsymbol{T}_\infty$ and definitions (A.6) of $C[\boldsymbol{x},t,\boldsymbol{\xi}|f], D[\boldsymbol{x},t,\boldsymbol{\xi}|f]$ and $E[\boldsymbol{x},t,\boldsymbol{\xi}|f]$ (wherein $f(t)=v_i^\varepsilon(\boldsymbol{\xi},t)$ according to A.2b), it is a simple matter to show that

$$\boldsymbol{T}_\infty(\boldsymbol{x},t,\boldsymbol{\xi};\boldsymbol{n}) \star \boldsymbol{v}^\varepsilon(\boldsymbol{\xi},t) = \frac{1}{\varepsilon^2}\boldsymbol{T}_{\infty,\varepsilon}(\bar{\boldsymbol{x}},t,\bar{\boldsymbol{\xi}};\boldsymbol{n}) \star \bar{\boldsymbol{v}}^\varepsilon(\bar{\boldsymbol{\xi}},t) \tag{A.17}$$

where $\boldsymbol{T}_{\infty,\varepsilon}$ is defined by (A.4c) and (A.6) with wave velocities $c_{\mathrm{L}}, c_{\mathrm{T}}$ replaced by rescaled values $c_{\mathrm{L}}/\varepsilon$ and $c_{\mathrm{T}}/\varepsilon$. Equation (A.17) and scaling (17) then imply

$$⨍_{\Gamma_\varepsilon(z)} \boldsymbol{T}_\infty(\boldsymbol{x},t,\boldsymbol{\xi};\boldsymbol{n}) \star \boldsymbol{v}^\varepsilon(\boldsymbol{\xi},t)\ \mathrm{d}S_\xi = ⨍_{\mathcal{S}} \boldsymbol{T}_{\infty,\varepsilon}(\bar{\boldsymbol{x}},t,\bar{\boldsymbol{\xi}};\boldsymbol{n}) \star \bar{\boldsymbol{v}}^\varepsilon(\bar{\boldsymbol{\xi}},t)\ \mathrm{d}\bar{S}_{\bar{\xi}} \tag{A.18}$$

Moreover, owing to the boundedness (A.9) of the complementary Green'a tensor $\boldsymbol{U}_{\mathrm{C}}$, one has, upon using again coordinate scaling (16):

$$⨍_{\Gamma_\varepsilon(z)} \boldsymbol{T}_{\mathrm{C}}(\boldsymbol{x},t,\boldsymbol{\xi};\boldsymbol{n}) \star \boldsymbol{v}^\varepsilon(\boldsymbol{\xi},t)\ \mathrm{d}S_\xi = O(\varepsilon^2)\|\bar{\boldsymbol{v}}^\varepsilon(\cdot,t)\| \tag{A.19}$$

where $\|\bar{\boldsymbol{v}}^\varepsilon(\cdot,t)\|$ is a norm of $\bar{\boldsymbol{\xi}} \mapsto \bar{\boldsymbol{v}}^\varepsilon(\bar{\boldsymbol{\xi}},t)$, e.g. its L^2-norm over $\mathcal{S}$. Lemma 2 then follows from combining (A.18) and (A.19).

Proof of Lemma 3. The proposed ansatz (20) is, by assumption in Lemma 1, Lipschitz-continuous w.r.t. t. It is therefore appropriate to investigate the behavior of $\boldsymbol{T}_\infty$ as defined by (A.4c) and (A.6) for a Lipschitz-continuous time-modulation f. Proceeding along the lines of Lemma 1, and in particular invoking again the decomposition $f(\tau) = f(t) + (f(\tau)-f(t)) = f(t)+\Delta f(\tau) =$, one has

$$\begin{aligned}
C[\bar{\boldsymbol{x}},t,\bar{\boldsymbol{\xi}}|f] &= \kappa^2 f(t) + C[\bar{\boldsymbol{x}},t,\bar{\boldsymbol{\xi}}|\Delta f] \\
D[\bar{\boldsymbol{x}},t,\bar{\boldsymbol{\xi}}|f] &= -\kappa^2 f(t) + D[\bar{\boldsymbol{x}},t,\bar{\boldsymbol{\xi}}|\Delta f] \\
E[\bar{\boldsymbol{x}},t,\bar{\boldsymbol{\xi}}|f] &= -\frac{3}{2}(1-\kappa^2) f(t) + E[\bar{\boldsymbol{x}},t,\bar{\boldsymbol{\xi}}|\Delta f]
\end{aligned} \tag{A.20}$$

Substituting the above values into (A.4c) and (A.6), one obtains the decomposition

$$\boldsymbol{T}_\infty[\bar{\boldsymbol{x}},t,\bar{\boldsymbol{\xi}}|f] = \boldsymbol{T}_\infty(\bar{\boldsymbol{x}},\bar{\boldsymbol{\xi}};\boldsymbol{n}) f(t) + \boldsymbol{T}_\infty[\bar{\boldsymbol{x}},t,\bar{\boldsymbol{\xi}}|\Delta f] \tag{A.21}$$

with $\boldsymbol{T}_\infty(\bar{\boldsymbol{x}},\bar{\boldsymbol{\xi}};\boldsymbol{n})$, the traction associated with the elastostatic Kelvin solution $\boldsymbol{U}_\infty(\bar{\boldsymbol{x}},\bar{\boldsymbol{\xi}})$, given by

$$\boldsymbol{T}_\infty(\bar{\boldsymbol{x}},\bar{\boldsymbol{\xi}};\boldsymbol{n}) = \frac{1}{4\pi\bar{r}^2}\Big[\kappa^2\big(\hat{\bar{\boldsymbol{r}}}\otimes\boldsymbol{n} - \boldsymbol{n}\otimes\hat{\bar{\boldsymbol{r}}} - (\hat{\bar{\boldsymbol{r}}}\cdot\boldsymbol{n})\boldsymbol{I}\big) + 3(\kappa^2-1)(\hat{\bar{\boldsymbol{r}}}\cdot\boldsymbol{n})\hat{\bar{\boldsymbol{r}}}\otimes\boldsymbol{n}\Big]. \tag{A.22}$$

Decomposition (A.21) is in particular applicable to $\boldsymbol{T}_{\infty,\varepsilon}[\ldots|f]$ defined by replacing velocities $c_{\mathrm{L}},\ c_{\mathrm{T}}$ by the rescaled values $c_{\mathrm{L}}/\varepsilon,\ c_{\mathrm{T}}/\varepsilon$ in $\boldsymbol{T}_{\infty}[\ldots|f]$. Owing to the assumed Lipschitz continuity of f, one easily shows that

$$\left\| \boldsymbol{T}_{\infty,\varepsilon}[\bar{\boldsymbol{x}},t,\bar{\boldsymbol{\xi}}|\Delta f] \right\| \leqslant C_{\mathrm{T}} K \varepsilon \qquad (\varepsilon \to 0)$$

where K is the Lipschitz constant of f and C_{T} is a constant. Consequently, using the fact that $\boldsymbol{T}_{\infty}(\bar{\boldsymbol{x}},\bar{\boldsymbol{\xi}};\boldsymbol{n})f(t)$ is unaffected by the wave velocity rescaling, decomposition (A.21) implies

$$\boldsymbol{T}_{\infty,\varepsilon}[\bar{\boldsymbol{x}},t,\bar{\boldsymbol{\xi}}|f] = \boldsymbol{T}_{\infty}(\bar{\boldsymbol{x}},\bar{\boldsymbol{\xi}};\boldsymbol{n})f(t) + o(1) \qquad (\varepsilon \to 0)$$

Lemma 3 then follows from equating $f(t)$ to the components of $\varepsilon\boldsymbol{\mathcal{V}}(\bar{\boldsymbol{\xi}}) : \boldsymbol{\sigma}[\boldsymbol{u}](\boldsymbol{z},t)$, according to (A.2b), in the above estimate.

Appendix A.3 3-D Scalar wave equation

The reference domain $\Omega \subset \mathbb{R}^3$ is now filled by an acoustic fluid characterized by the wave velocity c. The acoustic pressure field u_B generated by given excitations $\bar{p}(\boldsymbol{\xi},t)$ (proportional to normal wall acceleration) and $\bar{u}(\boldsymbol{\xi},t)$ (applied pressure) in the presence of a (possibly multiply-connected) sound-hard obstacle occupying a region B bounded by Γ is governed by the following set of equations:

$$\mathcal{P}(B) : \left\{ \begin{array}{ll} \big[\mathcal{L}_c u_B\big](\boldsymbol{\xi},t) = 0 & (\boldsymbol{\xi}\in\Omega, t\geqslant 0) \\ q[u_B](\boldsymbol{\xi},t) = 0 & (\boldsymbol{\xi}\in\Gamma, t\geqslant 0) \\ q[u_B](\boldsymbol{\xi},t) = \bar{p}(\boldsymbol{\xi},t) & (\boldsymbol{\xi}\in S_{\mathrm{N}}, t\geqslant 0) \\ u_B(\boldsymbol{\xi},t) = \bar{u}(\boldsymbol{\xi},t) & (\boldsymbol{\xi}\in S_{\mathrm{D}}, t\geqslant 0) \\ u_B(\boldsymbol{\xi},0) = \dot{u}_B(\boldsymbol{\xi},0) = 0 & (\boldsymbol{\xi}\in\Omega) \end{array} \right. \tag{A.23}$$

where $w \mapsto q[w] = \boldsymbol{\nabla} w \cdot \boldsymbol{n}$ is the normal derivative operator and $\mathcal{L}_c$, defined by

$$\left[\mathcal{L}_c w\right](\boldsymbol{\xi},t) = \Delta w(\boldsymbol{\xi},t) - \frac{1}{c^2}\ddot{w}(\boldsymbol{\xi},t) \tag{A.24}$$

is the governing partial differential operator of linear acoustics. Objective functions of format (5), with densities now having the form $\varphi\big[u_B(\boldsymbol{\xi},t),\ \boldsymbol{\xi},t\big]$, are again considered. Define a small scatterer $B_\varepsilon(\boldsymbol{z})$ of size ε as in Sec. 3, and let u denote the free field (which solves $\mathcal{P}(\emptyset)$) and v^ε the scattered field (such that the total field $u^\varepsilon = u + v^\varepsilon$ solves problem $\mathcal{P}(B_\varepsilon(\boldsymbol{z}))$). The governing integral equation for the scattered field v^ε reads

$$\frac{1}{2}v^\varepsilon(\boldsymbol{x},t) + \fint_{\Gamma_\varepsilon(z)} H[\boldsymbol{x},t,\boldsymbol{\xi};\boldsymbol{n}|v^\varepsilon(\boldsymbol{\xi},t)]\ \mathrm{d}S_\xi = -\int_{\Gamma_\varepsilon(z)} G[\boldsymbol{x},t,\boldsymbol{\xi};\boldsymbol{n}|q[u](\boldsymbol{\xi},t)]\ \mathrm{d}S_\xi \qquad (\boldsymbol{x}\in\Gamma_\varepsilon(\boldsymbol{z}),\ t\geqslant 0), \tag{A.25}$$

where the time-modulated Green's function $G[\boldsymbol{x},t,\boldsymbol{\xi}|f]$ solves the boundary-initial value problem

$$\begin{array}{ll} \mathcal{L}_{c,\xi} G[\boldsymbol{x},t,\boldsymbol{\xi}|f] = 0 & (\boldsymbol{\xi}\in\Omega, t\geqslant 0) \\ G[\boldsymbol{x},t,\boldsymbol{\xi}|f] = 0 & (\boldsymbol{\xi}\in S_{\mathrm{D}}, t\geqslant 0), \\ H[\boldsymbol{x},t,\boldsymbol{\xi}|f] = 0 & (\boldsymbol{\xi}\in S_{\mathrm{N}}, t\geqslant 0), \\ G[\boldsymbol{x},0,\boldsymbol{\xi}|f] = \dot{G}[\boldsymbol{x},0,\boldsymbol{\xi}|f] = 0 & (\boldsymbol{\xi}\in\Omega) \end{array} \tag{A.26}$$

and with $H[\boldsymbol{x},t,\boldsymbol{\xi};\boldsymbol{n}|f] = \boldsymbol{\nabla}_\xi G[\boldsymbol{x},t,\boldsymbol{\xi}|f]\cdot\boldsymbol{n}(\boldsymbol{\xi})$. Moreover, let $G_\infty[\boldsymbol{x},t,\boldsymbol{\xi}|f]$ denote the time-modulated *full-space* fundamental solution, given by (Eringen and Suhubi, 1975)

$$G_\infty[\boldsymbol{x},t,\boldsymbol{\xi}|f] = \frac{1}{4\pi r} f\Big(t - \frac{r}{c}\Big) \tag{A.27}$$

$$\boldsymbol{\nabla}_\xi G_\infty[\boldsymbol{x},t,\boldsymbol{\xi}|f] = -\frac{1}{4\pi r^2}\Big[f\Big(\boldsymbol{\xi},t-\frac{r}{c}\Big) + \frac{r}{c}\dot{f}\Big(t-\frac{r}{c}\Big)\Big]\hat{\boldsymbol{r}} \tag{A.28}$$

and define the complementary Green's function G_{C}, bounded in the limit $\boldsymbol{\xi} \to \boldsymbol{x}$, by $G_{\mathrm{C}}[\boldsymbol{x}, t, \boldsymbol{\xi}|f] = G[\boldsymbol{x}, t, \boldsymbol{\xi}|f] - G_\infty[\boldsymbol{x}, t, \boldsymbol{\xi}|f]$. The counterparts of Lemmas 1 and 2 then correspond to estimate

$$\int_{\Gamma_\varepsilon(z)} G(\boldsymbol{x}, t, \boldsymbol{\xi}) \star q[u] \, \mathrm{d}S_\xi = \varepsilon \Big\{ \int_{\mathcal{S}} G_\infty(\bar{\boldsymbol{x}}, \bar{\boldsymbol{\xi}}) \otimes \boldsymbol{n}(\bar{\boldsymbol{\xi}}) \, \mathrm{d}\bar{S}_{\bar{\xi}} \Big\} \cdot \boldsymbol{\nabla} u(\boldsymbol{z}, t) + o(\varepsilon), \tag{A.29}$$

assuming $\tau \mapsto \boldsymbol{\nabla} u(\boldsymbol{x}, \tau)$ is Lipschitz-continuous and differentiable in a neighbourhood of $\tau = t$, and

$$⨍_{\Gamma_\varepsilon(z)} H[\boldsymbol{x}, t, \boldsymbol{\xi}; \boldsymbol{n}|v^\varepsilon(\boldsymbol{\xi}, t)] \, \mathrm{d}S_\xi = \int_{\mathcal{S}} H_{\infty,\varepsilon}(\bar{\boldsymbol{x}}, \bar{\boldsymbol{\xi}}; \boldsymbol{n}) \bar{v}^\varepsilon(\bar{\boldsymbol{\xi}}, t) \, \mathrm{d}\bar{S}_{\bar{\xi}} + o(\|\bar{v}^\varepsilon\|) \quad (\varepsilon \to 0) \tag{A.30}$$

(with $H_\infty(\bar{\boldsymbol{x}}, \bar{\boldsymbol{\xi}}; \boldsymbol{n}) = \boldsymbol{\nabla}_{\bar{\xi}} G_\infty(\bar{\boldsymbol{x}}, \bar{\boldsymbol{\xi}}) \cdot \boldsymbol{n}(\boldsymbol{\xi})$, $H_{\infty,\varepsilon}$ defined by (A.28) with c replaced with c/ε, and $\bar{v}^\varepsilon(\bar{\boldsymbol{\xi}}, t)$ defined by $\bar{v}^\varepsilon(\bar{\boldsymbol{\xi}}, t) = v^\varepsilon(\boldsymbol{\xi}, t)$ with $\bar{\boldsymbol{\xi}}$ and $\boldsymbol{\xi}$ related through (16)). Estimates (A.29) and (A.30), established following the steps used for Lemmas 1 and 2, suggest the following asymptotic behavior for $v^\varepsilon(\boldsymbol{\xi}, t)$:

$$\bar{v}^\varepsilon(\bar{\boldsymbol{\xi}}, t) = \varepsilon \boldsymbol{\mathcal{V}}(\bar{\boldsymbol{\xi}}, t) \cdot \boldsymbol{\nabla} u(\boldsymbol{z}, t) + o(\varepsilon) \quad (\boldsymbol{\xi} \in \Gamma_\varepsilon(\boldsymbol{z}), \bar{\boldsymbol{\xi}} \in \mathcal{S}) \tag{A.31}$$

Upon substituting (A.31) into the right-hand side of (A.30), making use of the assumed Lipschitz continuity of $\tau \mapsto \boldsymbol{\nabla} u(\boldsymbol{x}, \tau)$, and retaining only the leading $O(\varepsilon)$ contributions as $\varepsilon \to 0$ according to (A.29) and (A.30), $\boldsymbol{\mathcal{V}}$ is readily found to verify an integral equation that corresponds to the following canonical exterior problem for the vector Laplace equation:

$$\Delta_{\bar{\xi}} \boldsymbol{\mathcal{V}}(\bar{\boldsymbol{\xi}}) = \boldsymbol{0} \quad (\bar{\boldsymbol{\xi}} \in \mathbb{R}^3 \setminus \mathcal{B}), \qquad \boldsymbol{\nabla}_{\bar{\xi}} \boldsymbol{\mathcal{V}}(\bar{\boldsymbol{\xi}}) \cdot \boldsymbol{n}(\bar{\boldsymbol{\xi}}) = -\boldsymbol{n}(\bar{\boldsymbol{\xi}}) \quad (\bar{\boldsymbol{\xi}} \in \mathcal{S}) \tag{A.32}$$

The scattered field v^ε at any point of S^{obs} is then found (inserting (A.31) into the integral representation formula associated with integral equation (A.25)) to have the expansion

$$v^\varepsilon(\boldsymbol{x}, t) = \varepsilon^3 |\mathcal{B}| \big\{ \boldsymbol{\nabla}_\xi G(\boldsymbol{x}, t, \boldsymbol{z}) \star [\boldsymbol{A} \cdot \boldsymbol{\nabla} u](\boldsymbol{z}, t) + \rho \dot{\boldsymbol{U}}(\boldsymbol{x}, t, \boldsymbol{z}) \star \dot{\boldsymbol{u}}(\boldsymbol{z}, t) \big\} + o(\varepsilon^3) \tag{A.33}$$

where the constant second-order polarization tensor $\boldsymbol{A} = \boldsymbol{A}(\mathcal{B})$ depends only on $\mathcal{B}$ and is defined by

$$\boldsymbol{A} = \boldsymbol{I} - \frac{1}{|\mathcal{B}|} \Big\{ \int_{\mathcal{S}} \boldsymbol{n}(\bar{\boldsymbol{\xi}}) \otimes \boldsymbol{\mathcal{V}}(\bar{\boldsymbol{\xi}}) \, \mathrm{d}\bar{S}_{\bar{\xi}} \Big\} \tag{A.34}$$

Finally, upon defining the adjoint solution $\hat{u}$ as the solution of the initial-boundary value problem

$$\begin{cases} \big[\mathcal{L}_c \hat{u}\big](\boldsymbol{\xi}, t) = 0 & (\boldsymbol{\xi} \in \Omega, 0 \leqslant t \leqslant T), \\ q[\hat{u}](\boldsymbol{\xi}, t) = \dfrac{\partial \varphi}{\partial u}[u(\boldsymbol{\xi}, T-t), \boldsymbol{\xi}, T-t] & (\boldsymbol{\xi} \in S^{\mathrm{obs}}, 0 \leqslant t \leqslant T), \\ q[\hat{u}](\boldsymbol{\xi}, t) = 0 & (\boldsymbol{\xi} \in S_{\mathrm{N}} \backslash S^{\mathrm{obs}}, 0 \leqslant t \leqslant T), \\ \hat{u}(\boldsymbol{\xi}, t) = 0 & (\boldsymbol{\xi} \in S_{\mathrm{D}}, 0 \leqslant t \leqslant T), \\ \hat{u}(\boldsymbol{\xi}, 0) = \dot{\hat{u}}(\boldsymbol{\xi}, 0) = 0 & (\boldsymbol{\xi} \in \Omega), \end{cases} \tag{A.35}$$

using reciprocity identity (29) suitably modified for linear acoustics, and exploiting the relevant boundary conditions, expansion (11) with $\boldsymbol{u}$ and $\boldsymbol{v}^\varepsilon$ respectively replaced with u and v^ε yields

$$\begin{aligned} \eta(\varepsilon)|\mathcal{B}|\mathbb{T}(\boldsymbol{z}, T) + o\big(\eta(\varepsilon)\big) &= \int_0^T \int_{S^{\mathrm{obs}}} \frac{\partial \varphi}{\partial u}[u(\boldsymbol{\xi}, t), \boldsymbol{\xi}, t] v^\varepsilon(\boldsymbol{\xi}, t) \, \mathrm{d}S_\xi \, \mathrm{d}t \\ &= -\int_{\Gamma_\varepsilon(z)} \big\{ q[\hat{u}] \star v^\varepsilon + q[u] \star \hat{u} \big\}(\boldsymbol{\xi}, t) \, \mathrm{d}S_\xi \\ &= \varepsilon^3 |\mathcal{B}| \big\{ \boldsymbol{\nabla} \hat{u} \star (\boldsymbol{A} \cdot \boldsymbol{\nabla} u) + \frac{1}{c^2} \dot{\hat{u}} \star \dot{u} \big\}(\boldsymbol{z}, t) + o(\varepsilon^3) \end{aligned} \tag{A.36}$$

with the polarization tensor $\boldsymbol{A}$ still defined by (A.34). Hence, the TS $\mathbb{T}(\boldsymbol{z}, t)$ and leading behavior

$\eta(\varepsilon)$ are found to be given by

$$\mathbb{T}(\boldsymbol{z},t) = \big\{\, \boldsymbol{\nabla}\hat{u} \star (\boldsymbol{A}\cdot\boldsymbol{\nabla}u) + \frac{1}{c^2}\dot{\hat{u}} \star \dot{u}\big\}(\boldsymbol{z},t), \qquad \eta(\varepsilon) = \varepsilon^3 \tag{A.37}$$

Appendix A.4 Two-dimensional case

The time-modulated full-space fundamental solution is given by (Eringen and Suhubi, 1975)

$$G_\infty[\boldsymbol{x},t,\boldsymbol{\xi}|f] = \frac{1}{2\pi}\int_0^{\eta^\star(r,t)} \frac{1}{[\eta^2+r^2]^{1/2}} f\Big(t-\frac{[\eta^2+r^2]^{1/2}}{c}\Big)\,\mathrm{d}\eta \tag{A.38}$$

$$\boldsymbol{\nabla}_\xi G_\infty[\boldsymbol{x},t,\boldsymbol{\xi}|f] = -\frac{1}{2\pi}\boldsymbol{r}\int_0^{\eta^\star(r,t)} \bigg\{ \frac{1}{[\eta^2+r^2]^{3/2}} f\Big(t-\frac{[\eta^2+r^2]^{1/2}}{c}\Big) + \frac{1}{c[\eta^2+r^2]}\dot{f}\Big(t-\frac{[\eta^2+r^2]^{1/2}}{c}\Big)\bigg\}\,\mathrm{d}\eta \tag{A.39}$$

where $\boldsymbol{\xi},\boldsymbol{x}$ now denote points in the two-dimensional space spanned by $(\boldsymbol{e}_1,\boldsymbol{e}_2)$, and the upper bound $\eta^\star(r,t)$ of the above integrals stems from the causality condition $f(\tau)=0,\ \tau<0$ and is given by

$$\eta^\star(r,t) = [(ct)^2 - r^2]^{1/2} \tag{A.40}$$

Proof of lemma 1. Assume that $\tau \mapsto \boldsymbol{\nabla}\dot{u}(\boldsymbol{\xi},\tau)$ is bounded for $0\leqslant\tau\leqslant t$ uniformly in a neighbourhood $V(\boldsymbol{z})$ of $\boldsymbol{z}$, which implies that $\tau \mapsto \boldsymbol{\nabla}u(\boldsymbol{\xi},\tau)$ is Lipschitz-continuous for $0\leqslant\tau\leqslant t$ uniformly in $V(\boldsymbol{z})$. Hence, for some positive constant K, one has

$$\|\boldsymbol{\nabla}\dot{u}(\boldsymbol{\xi},\tau)\| \leqslant K, \quad \|\boldsymbol{\nabla}u(\boldsymbol{\xi},\tau)-\boldsymbol{\nabla}u(\boldsymbol{\xi},\tau')\| \leqslant K|\tau-\tau'| \qquad 0\leqslant\tau,\tau'\leqslant t,\ \boldsymbol{\xi}\in V(\boldsymbol{z}) \tag{A.41}$$

Here, the tail effect, i.e. the fact (reflected in the integration bounds of (A.38), (A.39), and typical of 2-D time-domain fundamental solutions) that a time-impulsive source generates at $(\boldsymbol{\xi},t)$ a nonzero response over a continuous time interval, entails a proof method that is slightly more involved than for the previously-addressed 3-D cases. First, the main quantity of interest is recast into a domain integral along the lines of Appendix A.1:

$$-\int_{\Gamma_\varepsilon(z)} G_\infty(\boldsymbol{x},t,\boldsymbol{\xi}) \star q[u](\boldsymbol{\xi},t)\,\mathrm{d}S_\xi = \int_{B_\varepsilon(z)} \big\{\, \boldsymbol{\nabla}_\xi G_\infty(\boldsymbol{x},t,\boldsymbol{\xi}) \star \boldsymbol{\nabla}u(\boldsymbol{\xi},t) + \frac{1}{c^2} G_\infty(\boldsymbol{x},t,\boldsymbol{\xi}) \star \ddot{u}(\boldsymbol{\xi},t)\,\big\}\,\mathrm{d}V_\xi \tag{A.42}$$

Now, setting $f(\tau) = f(t) + \Delta f(\tau)$ in (A.39) and equating $f(\tau)$ to the components of $\boldsymbol{\nabla}u(\boldsymbol{\xi},\tau)$ in the resulting equality, one obtains

$$\boldsymbol{\nabla}_\xi G_\infty(\boldsymbol{x},t,\boldsymbol{\xi}) \star \boldsymbol{\nabla}u(\boldsymbol{\xi},t) = G_\infty(\boldsymbol{x},\boldsymbol{\xi})\cdot\boldsymbol{\nabla}u(\boldsymbol{\xi},t) + \boldsymbol{\nabla}_\xi G_\infty(\boldsymbol{x},t,\boldsymbol{\xi}) \star \boldsymbol{\nabla}\Delta u(\boldsymbol{\xi},t), \tag{A.43}$$

where $G_\infty(\boldsymbol{x},\boldsymbol{\xi})$ is the static 2-D full-space Laplace fundamental solution, given by

$$G_\infty(\boldsymbol{x},\boldsymbol{\xi}) = -\frac{1}{2\pi}\boldsymbol{r}\int_0^{\eta^\star(r,t)} \frac{1}{[\eta^2+r^2]^{3/2}}\,\mathrm{d}\eta = -\frac{1}{2\pi}\ln r, \qquad \boldsymbol{\nabla}_\xi G_\infty(\boldsymbol{x},\boldsymbol{\xi}) = -\frac{1}{2\pi r^2}\boldsymbol{r} \tag{A.44}$$

(with the second equality established via analytical integration). Moreover, utilizing the assumed Lipschitz continuity of $t\mapsto\boldsymbol{\nabla}u(\boldsymbol{\xi},t)$ for bounding the last term in (A.43) yields (noting that $\eta^\star(r,t)\leqslant ct$)

$$\big|\,\boldsymbol{\nabla}_\xi G_\infty(\boldsymbol{x},t,\boldsymbol{\xi})\star\boldsymbol{\nabla}\Delta u(\boldsymbol{\xi},t)\,\big| \leqslant \frac{r}{2\pi}\frac{2K}{c}\int_0^{\eta^\star(r,t)} \frac{\mathrm{d}\eta}{\eta^2+r^2} = \frac{K}{\pi c}\tan^{-1}\Big[\frac{(ct)^2}{r^2}-1\Big]^{1/2} \leqslant \frac{K}{2c} \tag{A.45}$$

with the last inequality stemming from the fact that $-\pi/2 \leqslant \tan^{-1}x \leqslant \pi/2$ for any x. Next, introducing the scaled coordinates (16), one obtains (by virtue of $\boldsymbol{\nabla}_\xi G_\infty(\boldsymbol{x},\boldsymbol{\xi})$ being homogeneous

of degree -1 in $\boldsymbol{x}-\boldsymbol{\xi}$)

$$G_\infty(\boldsymbol{x},\boldsymbol{\xi})\cdot\boldsymbol{\nabla}u(\boldsymbol{\xi},t)=\frac{1}{\varepsilon}G_\infty(\bar{\boldsymbol{x}},\bar{\boldsymbol{\xi}})\cdot[\boldsymbol{\nabla}u(\boldsymbol{z},t)+o(1)] \tag{A.46}$$

Finally, upon integrating decomposition (A.43) over B_ε, applying estimates (A.45) and (A.46), and noting that $\mathrm{d}V_\xi=\varepsilon^2\,\mathrm{d}\bar{V}_{\bar{\xi}}$ for the present 2-D case, one obtains (with the last equality stemming from applying the divergence formula):

$$\begin{aligned}\int_{B_\varepsilon(z)}\boldsymbol{\nabla}_\xi G_\infty(\boldsymbol{x},t,\boldsymbol{\xi})\star\boldsymbol{\nabla}u(\boldsymbol{\xi},t)\,\mathrm{d}V_\xi&=\varepsilon\Big\{\int_{\mathcal{B}}\boldsymbol{\nabla}_{\bar{\xi}}G_\infty(\bar{\boldsymbol{x}},\bar{\boldsymbol{\xi}})\,\mathrm{d}\bar{V}_{\bar{\xi}}\Big\}\cdot\boldsymbol{\nabla}u(\boldsymbol{\xi},t)+o(\varepsilon)\\&=\varepsilon\Big\{\int_{\mathcal{S}}G_\infty(\bar{\boldsymbol{x}},\bar{\boldsymbol{\xi}})\otimes\boldsymbol{n}(\bar{\boldsymbol{\xi}})\,\mathrm{d}\bar{S}_{\bar{\xi}}\Big\}\cdot\boldsymbol{\nabla}u(\boldsymbol{\xi},t)+o(\varepsilon)\end{aligned} \tag{A.47}$$

Finally, assuming in addition that $\ddot{u}(\boldsymbol{\xi},\tau)$ is uniformly bounded, i.e. $|\ddot{u}(\boldsymbol{\xi},\tau)|\leqslant M$ for some positive constant M, for $\boldsymbol{\xi}\in V(\boldsymbol{z})$, $0\leqslant\tau\leqslant t$, one has

$$\begin{aligned}\big|\,G_\infty(\boldsymbol{x},t,\boldsymbol{\xi})\star\ddot{u}(\boldsymbol{\xi},t)\,\big|=\big|\,G_\infty[\boldsymbol{x},t,\boldsymbol{\xi}|\ddot{u}(\boldsymbol{\xi},t)]\,\big|&\leqslant\frac{M}{2\pi c^2}\int_0^{\eta^\star(r,t)}\frac{1}{[\eta^2+r^2]^{1/2}}\,\mathrm{d}\eta\\&=\frac{M}{2\pi c^2}\ln\big[ct+\eta^\star(r,t)\big]-\ln r\end{aligned} \tag{A.48}$$

which implies, for ε small enough to have $B_\varepsilon(\boldsymbol{z})\subset V(\boldsymbol{z})$ and after effecting scaling (16):

$$\Big|\int_{B_\varepsilon(z)}G_\infty(\boldsymbol{x},t,\boldsymbol{\xi})\star\ddot{u}(\boldsymbol{\xi},t)\,\mathrm{d}V_\xi\Big|\leqslant\frac{M}{2\pi c^2}\varepsilon O(\varepsilon\ln\varepsilon)=o(\varepsilon) \tag{A.49}$$

Hence, combining (A.47) and (A.49), one arrives at an estimate formally identical to (A.29) where of course $\mathcal{B}$ is now the unit disk and G_∞ the 2-D static fundamental solution.

Proof of lemma 2. Introducing the scaled coordinates (16) into (A.39), performing the change of variable $\eta=\varepsilon\bar{\eta}$ in the resulting integral and noting that its upper bound $\bar{\eta}^\star(\bar{r},t)$ is given by (A.40) with r and c respectively replaced by $\bar{r}$ and c/ε. The 2-D analog of Lemma 2 is then readily obtained by invoking again the decomposition $G[\boldsymbol{x},t,\boldsymbol{\xi}|f]=G_\infty[\boldsymbol{x},t,\boldsymbol{\xi}|f]+G_{\mathrm{C}}[\boldsymbol{x},t,\boldsymbol{\xi}|f]$ and noting that

$$\int_{\Gamma_\varepsilon(z)}H_{\mathrm{C}}[\boldsymbol{x},t,\boldsymbol{\xi}|v^\varepsilon(\boldsymbol{\xi},t)]\,\mathrm{d}S_\xi=\varepsilon\int_{\mathcal{S}}H_{\mathrm{C}}[\bar{\boldsymbol{x}},t,\bar{\boldsymbol{\xi}}|\bar{v}^\varepsilon(\bar{\boldsymbol{\xi}},t)]\,\mathrm{d}\bar{S}_{\bar{\xi}}=O(\varepsilon\|\bar{v}^\varepsilon(\cdot,t)\|).$$

Proof of lemma 3. The proposed ansatz (A.31) is, by assumption in Lemma 1, Lipschitz-continuous w.r.t. t, which leads to investigating the behavior of H_∞ as defined through (A.39) for a Lipschitz-continuous time-modulation f. Proceeding along the lines of Lemma 1, and in particular invoking yet again the decomposition $f(\tau)=f(t)+\Delta f(\tau)$, one finds

$$H_\infty[\bar{\boldsymbol{x}},t,\bar{\boldsymbol{\xi}}|f]=H_\infty(\bar{\boldsymbol{x}},\bar{\boldsymbol{\xi}})f(t)+H_\infty[\bar{\boldsymbol{x}},t,\bar{\boldsymbol{\xi}}|\Delta f]$$

where the cofactor $H_\infty(\bar{\boldsymbol{x}},\bar{\boldsymbol{\xi}})$ of $f(t)$, established via analytical integration, is the normal derivative of the static fundamental solution (A.44). Moreover, exploiting the Lipschitz-continuity of f in the now-familiar way leads to

$$\big|\,H_\infty[\bar{\boldsymbol{x}},t,\bar{\boldsymbol{\xi}}|\Delta f]\,\big|\leqslant\frac{\bar{r}}{2\pi c^2}\frac{2K}{c}\int_0^{\eta_\varepsilon^\star(\bar{r},t)}\frac{\mathrm{d}\bar{\eta}}{\bar{\eta}^2+\bar{r}^2}=\frac{K}{\pi c}\tan^{-1}\Big[1-\frac{(ct)^2}{\bar{r}^2}\Big]^{1/2}$$

Two-dimensional elastodynamics. The infinite-plane time-modulated fundamental solution for two-dimensional elastodynamics is given by (Eringen and Suhubi, 1975):

$$\boldsymbol{U}_\infty[\boldsymbol{x},t,\boldsymbol{\xi}|f] = \frac{1}{\rho c_{\mathrm{T}}^2} G_{\mathrm{T}\infty}[\boldsymbol{x},t,\boldsymbol{\xi}|f]\boldsymbol{I} + \frac{1}{4\pi\rho}\boldsymbol{\nabla}_\xi\boldsymbol{\nabla}_\xi\left\{\int_0^{t-r/c_{\mathrm{L}}} \tau G_{\mathrm{L}\infty}[\boldsymbol{x},t-\tau,\boldsymbol{\xi}|f]\,\mathrm{d}\tau - \int_0^{t-r/c_{\mathrm{T}}} \tau G_{\mathrm{T}\infty}[\boldsymbol{x},t-\tau,\boldsymbol{\xi}|f]\,\mathrm{d}\tau\right\} r \quad \text{(A.50)}$$

where $G_{\mathrm{L}\infty},\ G_{\mathrm{T}\infty}$ are defined by (A.38) with $c=c_{\mathrm{L}}$ and $c=c_{\mathrm{T}}$, respectively. Lemma 1 to 3 can then be established by adapting the proof for the scalar case, a task left to the reader.

Appendix B Summary of explicit formulae for polarization tensors

Explicit formulae for polarization tensors $\boldsymbol{\mathcal{A}}$ have been established in earlier works (e.g. Sokolowski and Zochowski, 1999; Garreau et al., 2001; Guzina and Bonnet, 2004) for many situations. Moreover, the recent book by Ammari and Kang (2007) presents a comprehensive study of the concept of polarization tensor in connection with small-defect asymptotics and homogenization. For the case of spherical or (resp. circular) cavities nucleating in 3D (resp. 2D) isotropic elastic bodies, one has $|\mathcal{B}|=4\pi/3$ (3D) or $|\mathcal{B}|=\pi$ (2D)

$$\boldsymbol{\mathcal{A}} = \frac{3(1-\nu)}{2\mu(7-\nu)}\left[5\boldsymbol{\mathcal{I}}^{\mathrm{sym}} - \frac{1+5\nu}{2(1+\nu)}\boldsymbol{I}\otimes\boldsymbol{I}\right] \qquad \text{(3D)} \qquad \text{(B.1a)}$$

$$\boldsymbol{\mathcal{A}} = \frac{1}{\mu(1+\nu)}\left[2\boldsymbol{\mathcal{I}}^{\mathrm{sym}} - \frac{2\nu^2-\nu+1}{2(1+\nu)(1-\nu)}\boldsymbol{I}\otimes\boldsymbol{I}\right] \qquad \text{(2D plane stress)} \qquad \text{(B.1b)}$$

$$\boldsymbol{\mathcal{A}} = \frac{1-\nu}{\mu}\left[2\boldsymbol{\mathcal{I}}^{\mathrm{sym}} - \frac{1}{2(1+\nu)}\boldsymbol{I}\otimes\boldsymbol{I}\right] \qquad \text{(2D plane strain)} \qquad \text{(B.1c)}$$

The polarization tensor associated with the nucleation of a small spherical elastic inclusion with assumed elastic constants $\mu^\star,\nu^\star$ is given (see Chikichev and Guzina, 2008) by

$$\boldsymbol{\mathcal{A}}^\star = \mathcal{A}_{\mathrm{dev}}\boldsymbol{\mathcal{I}}^{\mathrm{sym}} + \frac{1}{3}(\mathcal{A}_{\mathrm{sph}}-\mathcal{A}_{\mathrm{dev}})\boldsymbol{I}\otimes\boldsymbol{I} \qquad \text{(B.2)}$$

having set

$$\begin{cases} \mathcal{A}_{\mathrm{sph}} = -\dfrac{3(1-2\nu)}{2\mu(1+\nu)}\dfrac{(1-\nu)(\bar\chi-1)}{(1+\nu)(\bar\chi-1)+3(1-\nu)} \\ \mathcal{A}_{\mathrm{sph}} = -\dfrac{1}{2\mu}\dfrac{15(1-\nu)(\bar\mu-1)}{(8-10\nu)(\bar\mu-1)+15(1-\nu)} \end{cases} \quad \text{with} \quad \bar\chi = \frac{\mu^\star(1+\nu^\star)(1-2\nu)}{\mu(1+\nu)(1-2\nu^\star)},\ \ \bar\mu = \frac{\mu^\star}{\mu}$$

The second-order polarization tensor associated with the nucleation of a small spherical sound-hard obstacle in an acoustic medium is given by

$$\text{(a) } \boldsymbol{A} = \frac{3}{2}\boldsymbol{I} \quad \text{(3-D)}, \qquad \text{(b) } \boldsymbol{A} = 2\boldsymbol{I} \quad \text{(2-D)} \qquad \text{(B.3)}$$